Chapter 4

Synergistic effect of electrostatic and electrodynamic electrical stimulation on osteogenic responses

This chapter discusses the influence of formation of bioelectrets Ca and Zr co-doped $MgSiO_3$ *[*$Mg_{1-x}Ca_xSi_{1-x}Zr_xO_3$ *(x = 0 - 0.1, 0.2, 0.3, 0.4); MCSZO-X, X=0 – 4] and electrodynamic stimulation towards improving their osteogenic response. The effect of surface charge on the wettability, surface chemistry and leaching of ions (Mg, Ca, Zr and Ca) was examined using contact angle measurement, X-ray photoelectron spectroscopy (XPS), and inductively coupled plasma (ICP) analyses, respectively. Further, the combined effect of electrostatic charge and electrodynamic stimulation along with compositional modification on cell proliferation, adhesion and differentiation were analyzed. Further, the mechanism of enhanced cellular functionality was revealed by the measurement of intracellular* Ca^{2+}*.*

4.1. Characterization of MCSZO-X (X = 0 - 4) bioceramics

4.1.1. Densification and phase evaluation

The sintering temperatures for MCSZO0, MCSZO1, MCSZO2, MCSZO3, and MCSZO4 [MCSZO-X (X = 0 − 4)] have been optimized to be 1380, 1350, 1350, 1320, and 1320 ºC, respectively. The densification behavior of sintered MCSZO-X samples is represented in Figure. 4.1a. The XRD patterns of sintered MCSZO-X and HA samples are shown in Figure. 4.1b. The XRD patterns confirm the formation of orthorhombic (protoenstatite system) pure $MgSiO_3$ [JCPDS #76-1806] phase with space group as, Pbcn and lattice parameters as, a = 9.25 Å, b = 8.74 Å, c = 5.32 Å. Also, some minor peaks were indexed with JCPDS #72-0439 [(a = 9.68 Å, b = 9.73 Å, c = 5.20 Å), space group of P21/n] and JCPDS #19-0769 [(a = 9.60 Å, b = 8.81 Å, c = 5.16 Å), space group of P21/a], which correspond to monoclinic (Clinoenstatite system) $MgSiO_3$ structure and HA (# 09-0432), respectively [1-4]. The profile fitting of pure $MgSiO_3$ and MCSZO-X (X=1) was performed using full proof software to calculate the lattice parameters and to observe associated change in their values. The calculated lattice parameter value for pure $MgSiO_3$ (X=0) is (a=9.27, b= 8.75 and c=5.31 for orthorhombic structure and a=9.60, b=8.90 and c= 5.21for monoclinic structures) and the lattice parameter value for MCSZO-X (X= 1) is (a=9.61, b= 8.79 and c=5.33 for orthorhombic and a=9.66, b=8.81 and c= 6.15 for monoclinic structures).

The five polymorphic forms $MgSiO_3$ exists in two crystal structures, monoclinic and orthorhombic [5, 6]. The positions of peaks shifted towards lower 2θ values by increasing the concentration of Ca and Zr from 0 to 0.3 [Figure. 4.1c]. This is due to incorporation of Ca^{2+} ions (r = 1.34 Å) on smaller Mg^{2+} (r = 0.72 Å) at the A-site and Zr^{4+} ions (r = 0.74 Å) at smaller Si^{4+} (r = 0.40 Å) on the B-site [7, 8]. The doping of higher - ionic - radii Ca (1.00 Å) at the Mg (0.72 Å) site having smaller ionic radii and higher- ionic- radii Zr (0.74 Å) ion at the Si (0.42 Å) site having smaller ionic radii was confirmed by the phase analyses. It was observed that the peak position shifted towards lower 2θ values on increasing the concentration of Ca and Zr from 0 to 0.3. This was the result of lattice expansion that occurred within $MgSiO_3$ [9-12]. However, as the value of x increases from 0.3 to 0.4, the peak shifts toward a higher angle. Because of the presence of more Ca^{2+} at the Mg^{2+} site, the lattice contraction in MCSZO-X bioceramics occurs [9, 12-14]. Also, for compositions, x = 0.3 to x = 0.4, the presence of two additional minor phases of $CaSiO_3$ and $CaMgSiO_3$ (JCPDS # 19-0239) were observed during phase analyses. The development of secondary-phase (Mg_2SiO_3)complicates the synthesis of single phase $MgSiO_3$ [1, 14]. On increasing the concentration of Ca and Zr from 0.3 to 0.4, minor phases ($CaSiO_3$, Ca_2MgSiO_7, Mg_2SiO_4 and $CaMg(SiO_3)_2$ started to form.

The tolerance factor of complex perovskites ($A_{1-x}A_xB_{1-y}B_yO_3$) was calculated for the perovskite formation, structure distortion, and structural stability using Goldschmidt tolerance factor formula, for ABO_3 type perovskite [15].

$$T_f = \frac{(R_A+R_O)}{\sqrt{2}(R_B+R_O)} \tag{4.1}$$

In this formula, R_A, R_B, and R_O are the radii of A and B cation and anion, respectively. For complex perovskite $A_{1-x}A_xB_{1-y}B_yO_3$,

$$T_f = \frac{(1-x)R_{Mg^{2+}} + x\,R_{Ca^{2+}} + R_{O^{2-}}}{\sqrt{2}\,[(1-y)R_{Si^{4+}} + yR_{Zr^{4+}} + R_{O^{2-}}]} \tag{4.2}$$

Where, R_{Mg}, R_{Ca}, R_{Si}, and R_{Zr} are the ionic radii of Mg^{2+} (0.72 Å), Ca^{2+} (1.34 Å), Si^{4+} (0.40 Å), Zr^{4+} (0.74 Å) cations and O^{2-} (1. 40 Å), respectively [7, 8]. The values of tolerance factor are varying from 0.834 to 0.865, with increasing the concentration of Ca and Zr.

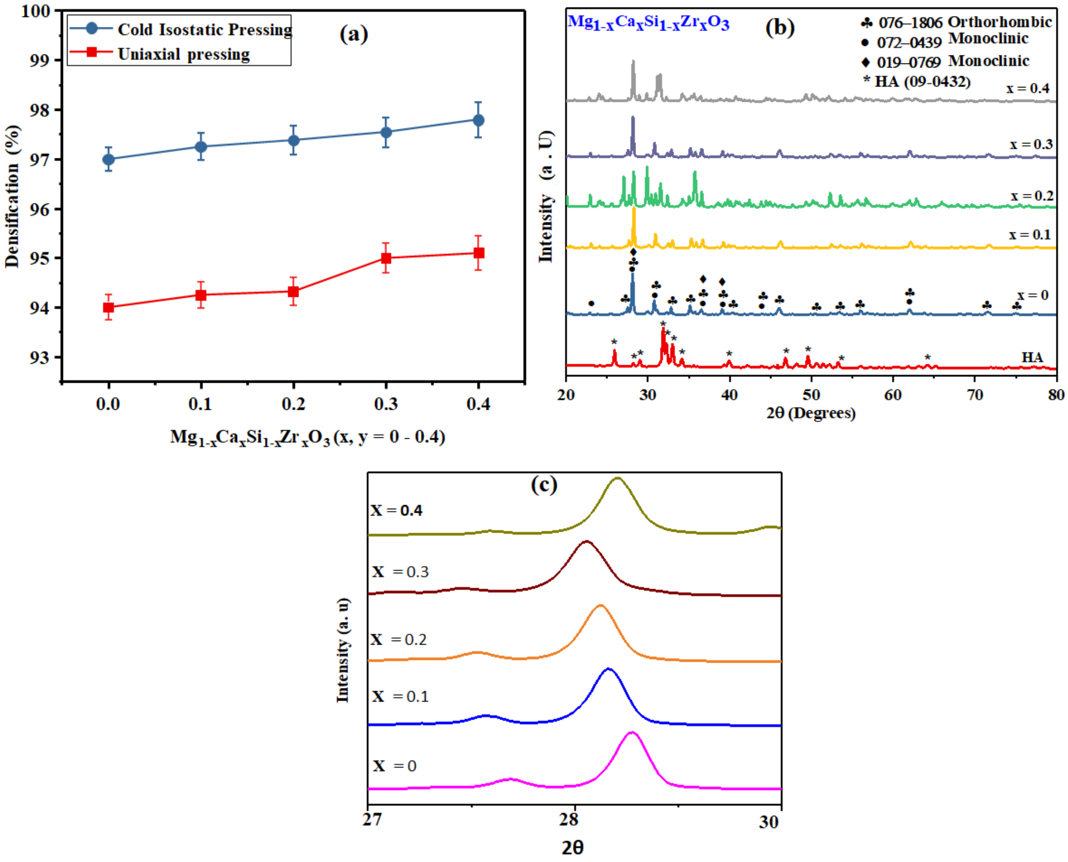

Figure 4.1. Densification and phase evolution of $Mg_{1-x}Ca_xSi_{1-x}Zr_xO_3$; MCSZO-X (X = 0− 4) samples, sintered at 1380 - 1320 °C. (a) The relative densities of sintered MCSZO-X samples. (b) XRD patterns for MCSZO-x (x = 0 − 0.4) samples, (c) Enlarged view of the most intense Bragg's peak in 2θ range of 27-30°.

4.1.2. Fourier transform infrared (FTIR) spectroscopy

FTIR spectra of all the sintered MCSZO-X and HA samples are presented in Figure. 4. 2. The stretching and bending vibrations, corresponding to Si-O are observed at 1052, 600, 500, and 470 cm^{-1}. The bending vibration of Si-O-Si is present at around 800 cm^{-1}, which confirms the formation of $MgSiO_3$ [16, 17]. Also, the strong vibrational band, corresponding to Si-O in silicate tetrahedral is observed at 682 cm^{-1}. The vibrational bands at 509 cm^{-1} and peak around 500 cm^{-1} are attributed to Ca-O stretching vibration and Mg-O stretching vibration, respectively [18-20]. The Zr-O stretching and bending vibrational bands are observed at 873 cm^{-1} [21, 22]. All the samples reveal the asymmetric stretching vibration for Si-O band at 1000 cm^{-1} [Figure. 4.2a][16]. The FTIR spectrum shows a band near 3451 cm^{-1} due to the presence of OH^- group, and band at 1608 cm^{-1} represents the bending vibration of OH^- group [Figure. 4.2b] [23, 24].

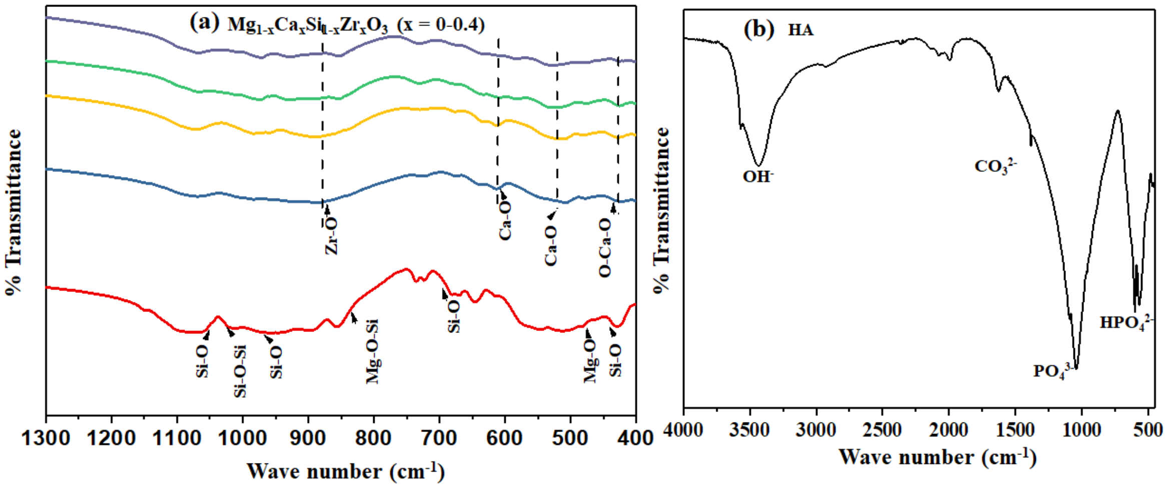

Figure 4.2. Fourier transform infrared (FTIR) spectra of (a) sintered $Mg_{1-x}Ca_xSi_{1-x}Zr_xO_3$ (MCSZO- X) (x = 0, 0.1, 0.2, 0.3, and 0.4) and (b) HA samples.

4.1.3. Microstructural analyses

The surface morphology and EDS spectra of fractured MCSZO-X samples are shown in Figure. 4.3(a – e). The brittle mode of fracture is evident in every sample.

A slight grain growth is observed with increasing the concentration (x= 0 to 0.4). The grain sizes of MCSZO- X samples are measured to be 1.69, 1.92, 1.98, 2.01, and 2.18 µm, respectively. The grain size of MCSZO-X samples significantly increases. From the above results, it is clearly observed that with the increase of the amount of Ca and Zr in MCSZO-X samples, grain size values are significantly increasing.

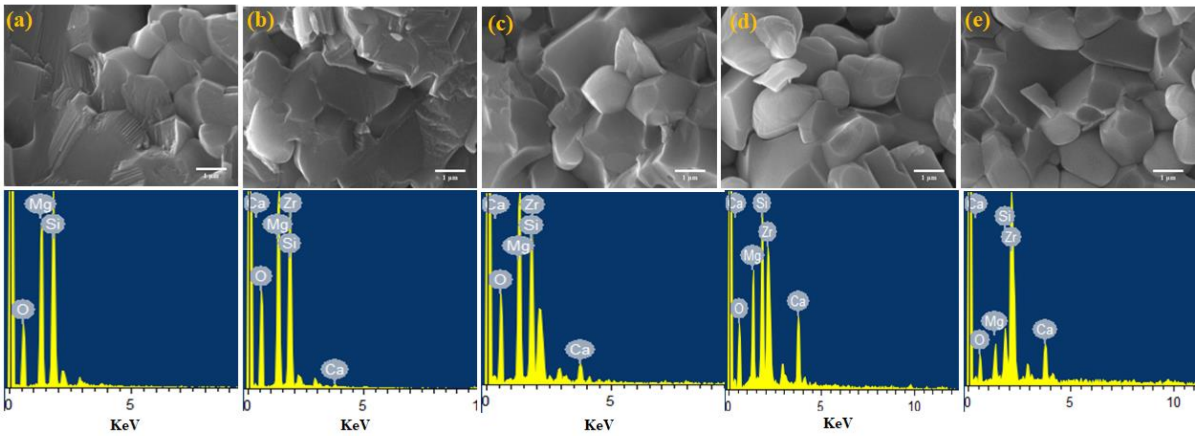

Figure 4.3. Scanning electron micrographs and energy dispersive X-ray spectroscopy (EDS) graphs for fractured $Mg_{1-x}Ca_xSi_{1-x}Zr_xO_3$ *samples: (a) x = 0, (b) x = 0.1, (c) x = 0.2, (d) x = 0.3, and (e) x = 0.4, sintered at 1380- 1320 °C.*

4.2. Leaching behavior

Figure. 4.4 (a-d) displays the concentration of various ions, leached from uncharged and MCSZO-X electrets samples after 7, 14, and 21 days of soaking in SBF. The results indicate the dissolution of Mg^{2+} and Si^{4+} ions from the $MgSiO_3$ sample as well as Ca/Zr-doped MCSZO-X samples. However, in pure $MgSiO_3$ ceramic, the concentrations of Mg^{2+} and Si^{4+} ions are higher than those of Ca/Zr doped MCSZO-X samples. However, with the increase of the concentrations of Ca and Zr in MCSZO-X samples, the concentration of Mg^{2+} and Si^{4+} decreases and the release rate of Ca^{2+} and Zr^{4+} ions increase.

The leaching of Ca^{2+} from MCSZO-X increases with increase in the soaking period from day 7 to 21 (33.3, 53.4, 85.0, 90.3 ppm to 42.4, 72.0, 120.8, 123.2 ppm, respectively).

It has been reported that the Ca^{2+} ions leached out faster than Mg^{2+} and Si^{4+} ions [25]. Such higher release of Ca^{2+} ions from the MCSZO-X samples might be due to the lower bonding strength of Ca-O, which causes easier dissociation of Ca^{2+} from the lattice structure in comparison to Si-O and Mg-O bonds [25].

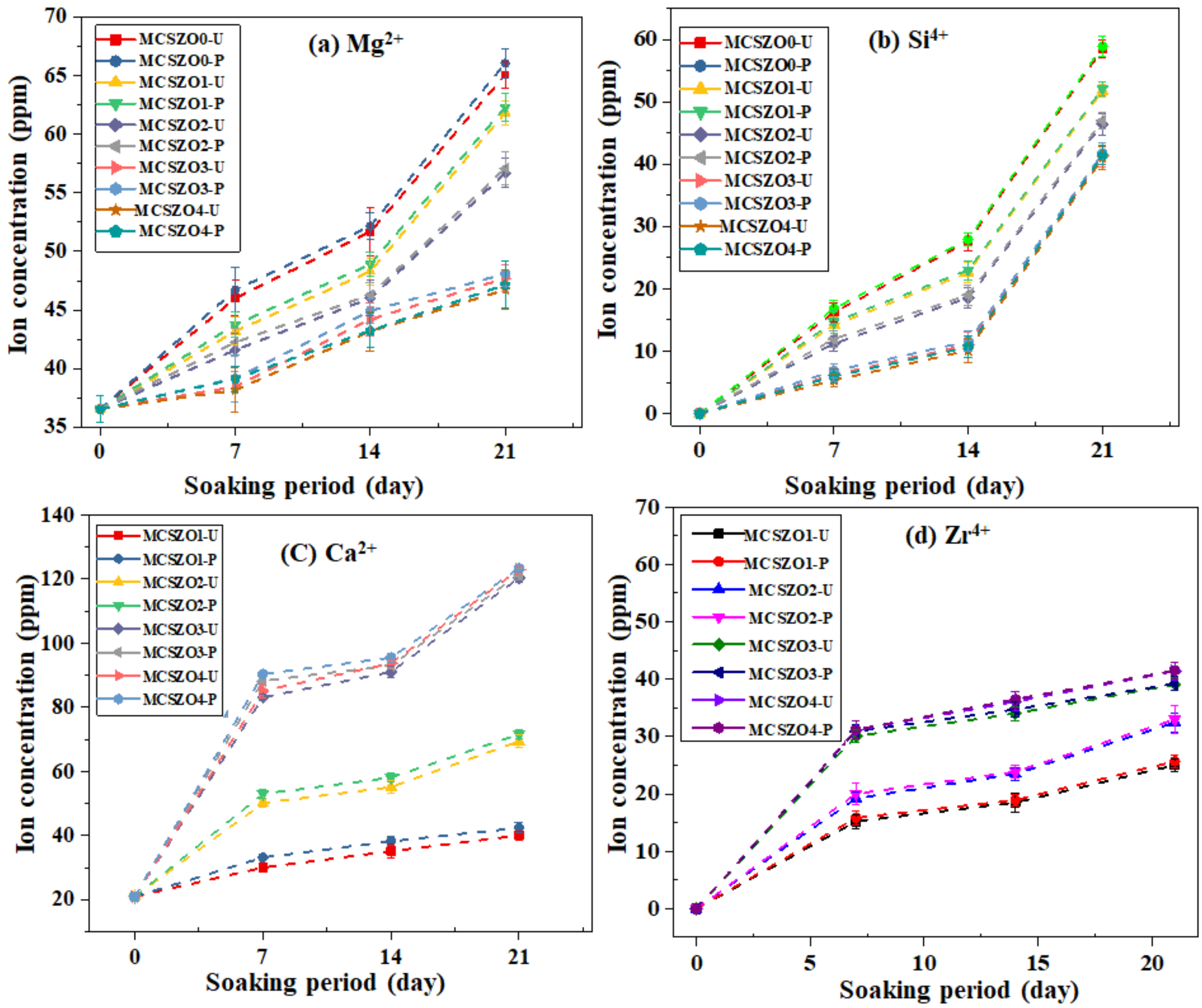

Figure 4.4. Leaching profile of Mg^{2+}, Si^{4+}, Ca^{2+}, Zr^{4+} ions from MCSZO- X (X = 0 - 4) samples in simulated body fluid (SBF). The graphs representing the changes in the concentrations of (a) Mg^{2+}, (b) Si^{4+}, (c) Ca^{2+} and (d) Zr^{4+} ions with respect to immersion period.

4.3. Contact angle measurement

The contact angle measurement was performed with DI water and DMEM media to examine the effect of development of electrets on the surface wettability [Figure. 4.5]. The contact angles of negatively charged electrets are significantly lower than those of uncharged and positive end of MCSZO-X and HA electret samples.

For DI water and culture media, the contact angle decreases from 45.5° to 25.6° and 40.1° to 25.1°, respectively, on negative end of electret. However, the composition, X = 3 shows the lowest contact angle i.e., 25.6° and 25.1°, on the negative end of electret in both, DI water and culture media, respectively. With increasing the content of Ca/Zr in $MgSiO_3$, the contact angle decreases. The improved surface hydrophilicity promotes the cell proliferation [26, 27].

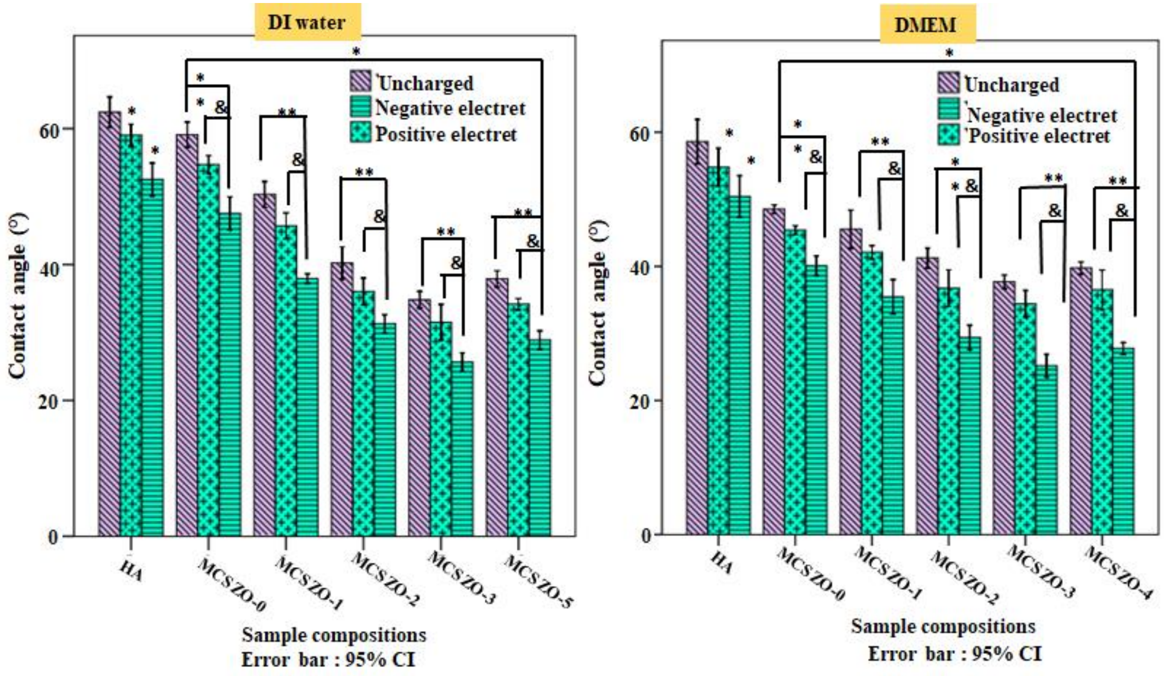

Figure 4.5. Values of Contact angle on the surface of uncharged and MCSZO-X (X = 0-4) electrets of samples using (a) Deionized (DI) water and (b) DMEM. Asterisk (*) denotes the significant variation in the mean values of water contact angles among the HA electret, and uncharged as well as MCSZO-X electret samples as compared to uncharged HA samples, (at $p \leq 0.05$). (**) and (#) marks indicate the significant variation in the mean values of water contact angles on MCSZO-X electrets with respect to the negative end of HA electret and uncharged MCSZO-X samples, respectively, at $p \leq 0.05$.

4.4. X-Ray photoelectron spectroscopic (XPS) analyses

XPS spectra of uncharged and MCSZO-X electret samples are shown in Figure 4.6 (a − e). The C1s peak shifted to the higher binding energy side by 0.07 eV, after electret formation. The XPS spectra, related to O 1s for both, uncharged and MCSZO-X electret samples, are shown in Figure. 4. 7 (a − j).

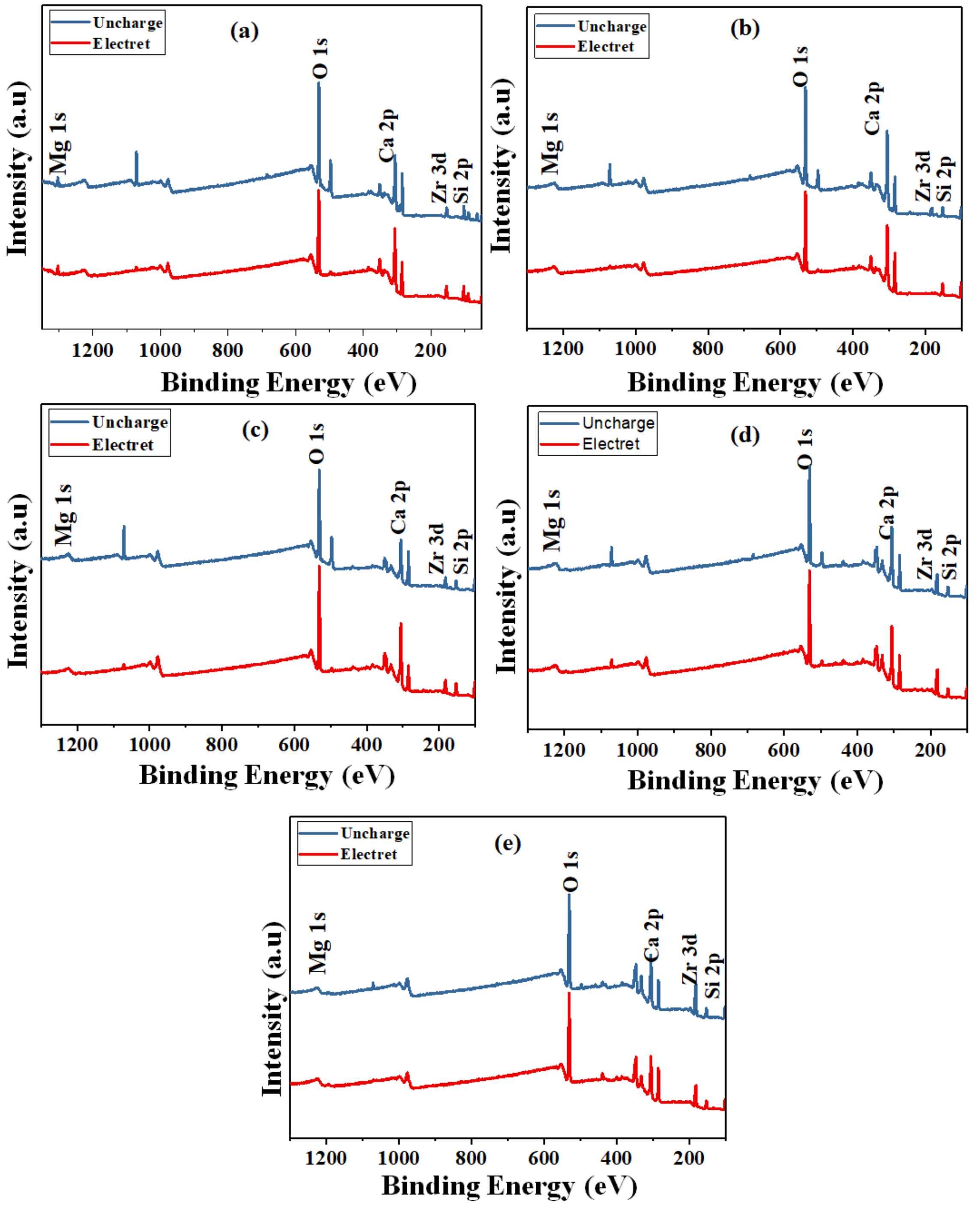

Figure 4.6. X-ray photoelectron spectroscopy (XPS) spectra of uncharged and MCSZO -X (X = 0 - 4) electret samples. XPS survey spectrum of uncharged and MCSZO -X electret samples, i.e., (a) MCSZO-0, (b) MCSZO-1, (c) MCSZO-2, (d) MCSZO-3, and (e) MCSZO-4, for Mg (1s), Ca (2p), Si (2p), Zr (3d), O (1s), and C (1s) orbital states.

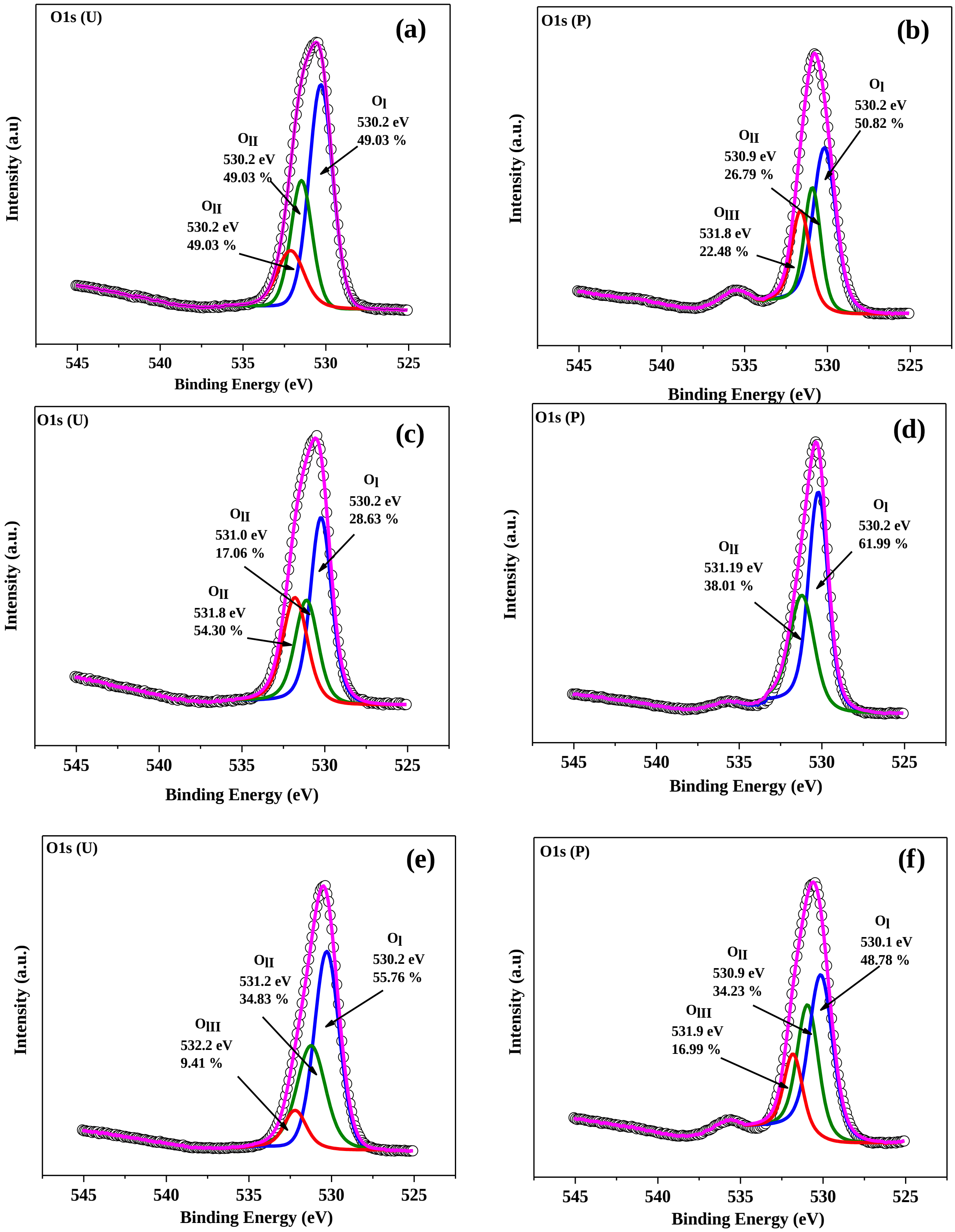
O1s (U)
(a)
OI
530.2 eV
49.03 %
OII
530.2 eV
49.03 %
OII
530.2 eV
49.03 %
Intensity (a.u)
545
540
535
530
525
Binding Energy (eV)
O1s (P)
(b)
OI
530.2 eV
50.82 %
OII
530.9 eV
26.79 %
OIII
531.8 eV
22.48 %
Intensity (a.u.)
545
540
535
530
525
Binding Energy (eV)
O1s (U)
(c)
OI
530.2 eV
28.63 %
OII
531.0 eV
17.06 %
OII
531.8 eV
54.30 %
Intensity (a.u.)
545
540
535
530
525
Binding Energy (eV)
O1s (P)
(d)
OI
530.2 eV
61.99 %
OII
531.19 eV
38.01 %
Intensity (a.u.)
545
540
535
530
525
Binding Energy (eV)
O1s (U)
(e)
OI
530.2 eV
55.76 %
OII
531.2 eV
34.83 %
OIII
532.2 eV
9.41 %
Intensity (a.u.)
545
540
535
530
525
Binding Energy (eV)
O1s (P)
(f)
OI
530.1 eV
48.78 %
OII
530.9 eV
34.23 %
OIII
531.9 eV
16.99 %
Intensity (a.u)
545
540
535
530
525
Binding Energy (eV)

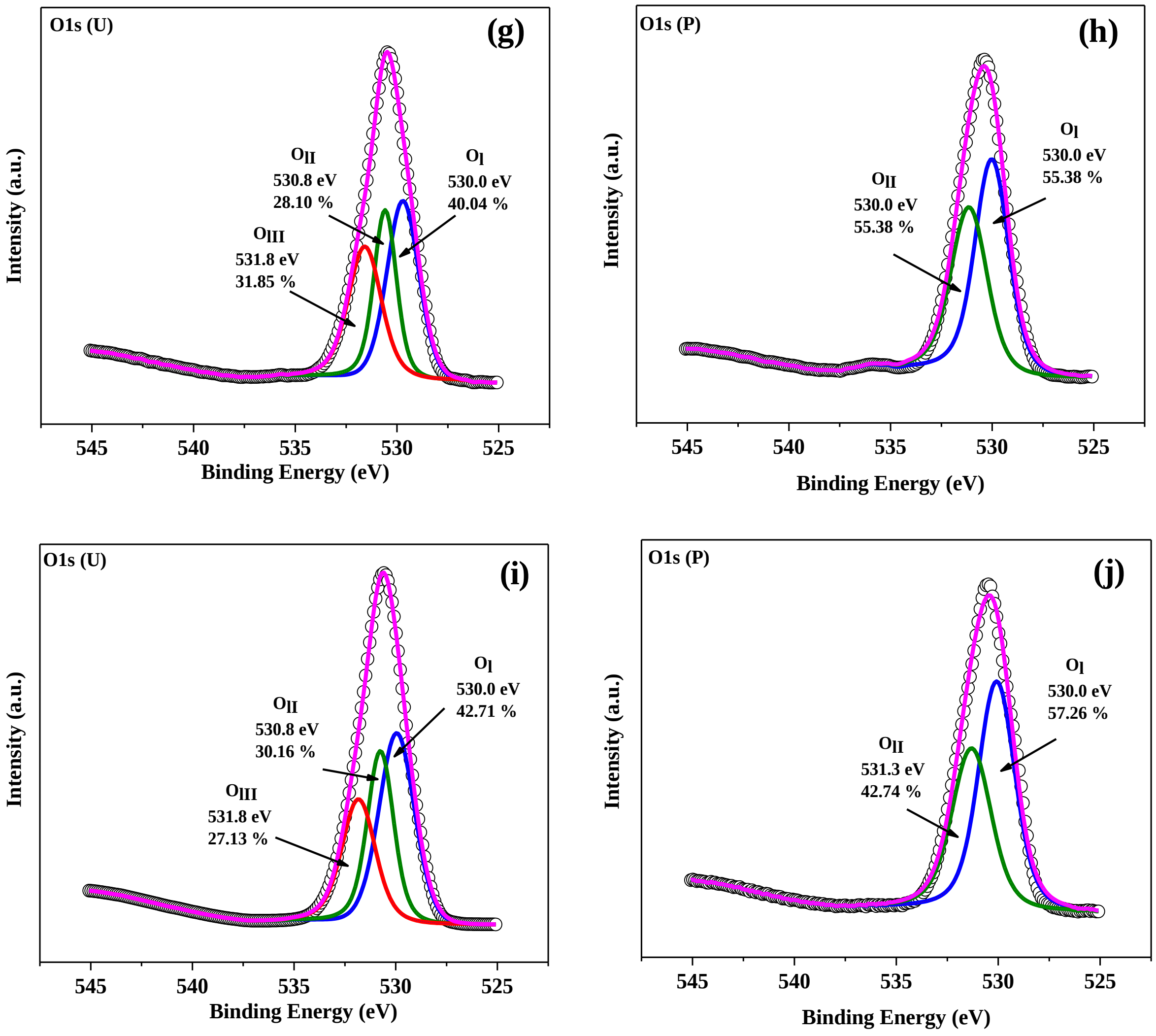

Figure 4.7. X-ray photoelectron spectroscopy (XPS) spectra of both, uncharged and electret surfaces of MCSZO-X (X = 0 - 4) samples, i.e., (a, b) MCSZO-0, (c,d) MCSZO-1, (e, f) MCSZO-2, (g, h) MCSZO-3, and (i, j) MCSZO-4, for O 1s. Representation of O 1s spectra for uncharged MCSZO-X, (a, c, e, g, i) and electrets of MCSZO-X, (b, d, f, h, j) samples, (X= 0 – 4).

Before doping, the binding energy of the Mg1s peak was constant at 1303.3 eV, while on doping of Ca and Zr, the peak shifted to a slightly higher binding energy of 1303.6 eV [Figure. 4.8] [28]. Such variation may be due to Mg, as it shows more electropositive bonding with the metal oxygen atoms [29].

The binding energy of Mg 1s peak remains unchanged after electret formation. In high-resolution Ca 2p XPS spectra, the binding energies of Ca2p$_{3/2}$ and Ca2p$_{1/2}$ for electret and uncharged samples are 346 ± 0.1 – 347 ± 0.1 eV and 350 ± 0.1 – 350.6 ± 0.1 eV, respectively [Figure 4.9]. The Ca2p peak region is overlapped by Mg auger peak (MgKLL); therefore, it is difficult to obtain an accurate intensity ratio of Ca2p$_{3/2}$ (346.6 eV) and Ca2p$_{1/2}$ (351 eV), as desired (~2) [30]. The spin-orbit doublet of Ca 2p and Zr 3d has been clearly observed with split energy gap in Ca2p$_{3/2}$ – Ca2p$_{1/2}$ and Zr3d$_{5/2}$ − Zr3d$_{1/2}$ of 3.5 and 2.3 eV, respectively [31, 32]. Since, Si 2p has a narrow peak split energy gap in Si 2p$_{3/2}$ – Si 2p$_{1/2}$ of 0.63 eV, which cannot be resolved at higher pass energy (50 eV), it is used during elemental analyses. Therefore, a single peak of Si 2p has been observed here. The Si 2p peak is centred at 101.3 eV which remains unchanged after electret formation [Figure. 4.10] [33].

During XPS analyses, it has been observed that in pure $MgSiO_3$ samples, the auger peak of MgKLL is evident [30]. The ratio of Ca2p$_{3/2}$ and MgKLL increases with the increased concentrations of Ca and Zr from 0.1 to 0.4 in $MgSiO_3$ for both, uncharged (0.989 to 0.99) and (0.988 to 0.999) MCSZO-X electret samples. The later peak at 350.4 eV can be allocated to MgKLL electrons, which superposes the Ca 2p spectrum [Figure. 4.9][30].

Zr 3d peaks also remain unchanged after electret formation, and the binding energies of Zr3d$_{7/2}$ and Zr3d$_{5/2}$ are 181.1 eV and 183.6 eV, respectively [Figure. 4.11][34]. Moreover, the XPS spectrum of O 1s peak for both, uncharged and electret samples are shown in Figure. 4. 7 (a − j). The O 1s peaks for all of the MCSZO-X samples are deconvoluted into three peaks: adsorbed oxygen sites (532.8 eV, O_A), oxygen deficient sites (531.7 eV), and lattice oxygen (530.2 eV, O_L), as shown in Figure. 4.7 (a – j) [35-37].

Among the O 1s orbitals in uncharged and MCSZO-X electret samples, the ratio of O_V/O_L (oxygen vacancy / lattice oxygen) increases with the increase in doping from X = 0 − 4 [Figure. 4.12].

The oxygen deficiency ($Mg_{1-x}Ca_xSi_{1-x}Zr_xO_{3-\delta}$) increased from 0.18 to 0.360 with increasing the concentration of Ca and Zr from 0.1 to 0.4 in $MgSiO_3$. Also, the O 1s spectra of $Mg_{1-x}Ca_xSi_{1-x}Zr_xO_3$ electret samples indicate that the electret surfaces have increased hydrophilicity, leading to improved cellular performance. The substitution of ions having larger ionic radii with those having smaller radii leads to the creation of oxygen vacancies [12]. It has been observed that this ratio ($O_V/O_{L)}$ is higher in the case of electret samples, as the formation of electrets enhances the oxygen deficient sites by forming the localized domain of electrons. It has been reported that the surface becomes hydrophilic due to the oxygen deficiency that induced active sites for the adsorption of water [38-41]. Overall, the peak positions of Mg, Ca, Si, and Zr elements in uncharged and MCSZO-X electret are the same, which reveal that the formation of electrets does not influence the surface chemistry of the MCSZO- X samples.

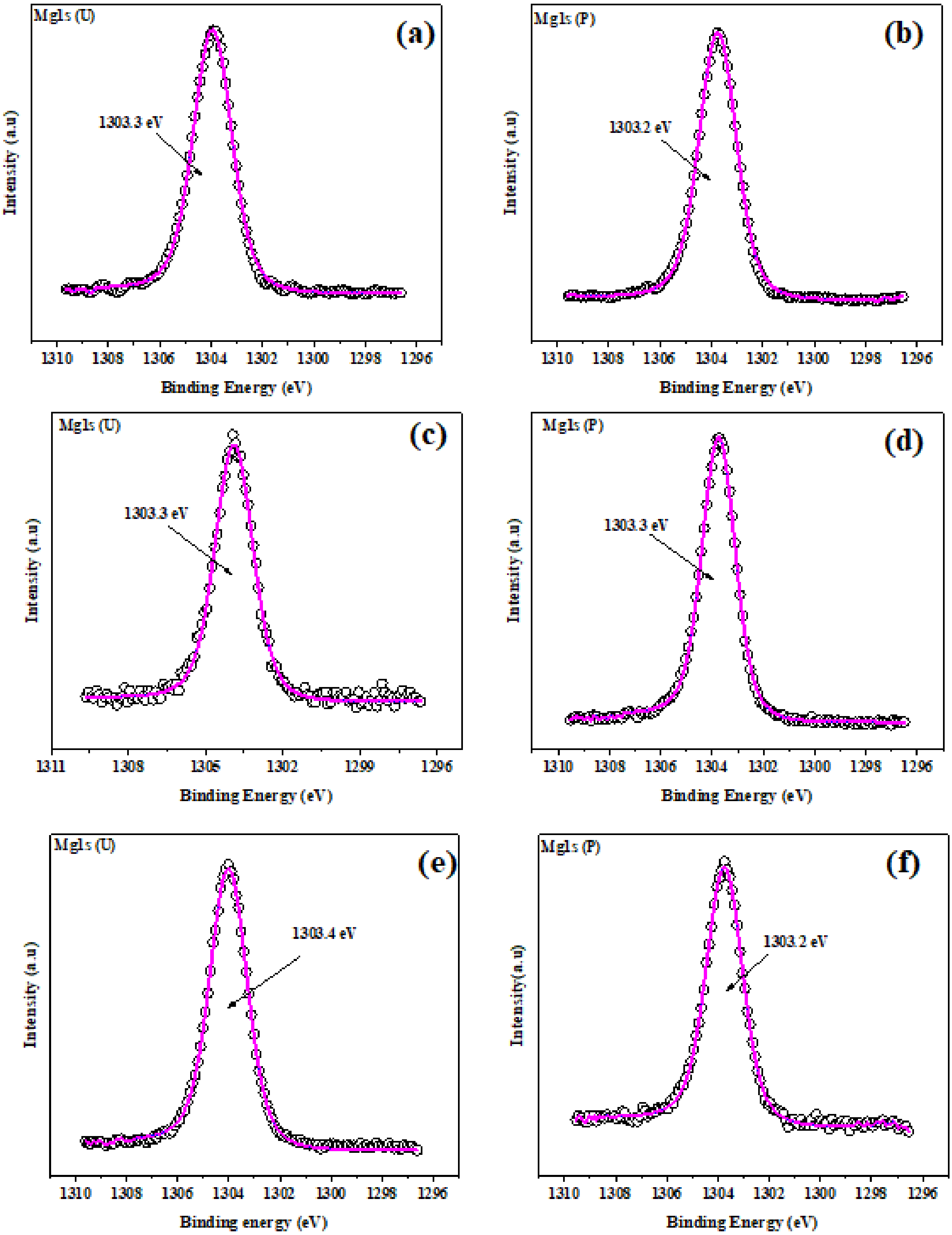
Mg1s (U)
(a)
1303.3 eV
Intensity (a.u)
1310 1308 1306 1304 1302 1300 1298 1296
Binding Energy (eV)
Mg1s (P)
(b)
1303.2 eV
Intensity (a.u)
1310 1308 1306 1304 1302 1300 1298 1296
Binding Energy (eV)
Mg1s (U)
(c)
1303.3 eV
Intensity (a.u)
1311 1308 1305 1302 1299 1296
Binding Energy (eV)
Mg1s (P)
(d)
1303.3 eV
Intensity (a.u)
1310 1308 1306 1304 1302 1300 1298 1296
Binding Energy (eV)
Mg1s (U)
(e)
1303.4 eV
Intensity (a.u)
1310 1308 1306 1304 1302 1300 1298 1296
Binding energy (eV)
Mg1s (P)
(f)
1303.2 eV
Intensity(a.u)
1310 1308 1306 1304 1302 1300 1298 1296
Binding Energy (eV)

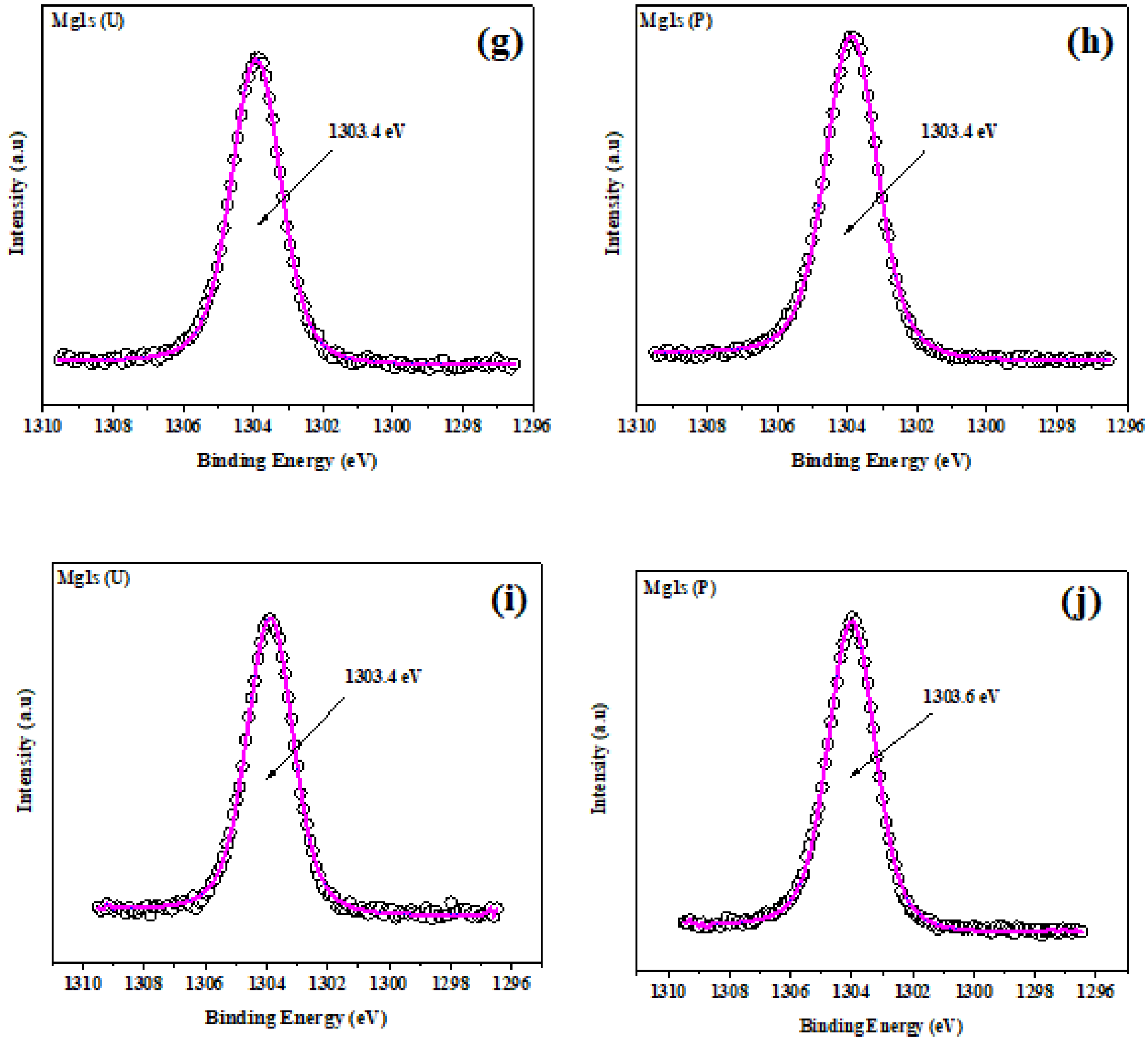

Figure 4.8 XPS spectra of both, uncharged and electret surfaces of MCSZO -X (X = 0 – 4) samples, i.e., (a, b) MCSZO-0, (c,d) MCSZO-1, (e, f) MCSZO-2, (g, h) MCSZO-3, and (i, j) MCSZO-4, for Mg 1s. Representation of Mg 1s spectra for uncharged MCSZO-X, (a, c, e, g, i), and electret of MCSZO-X, (b, d, f, h, j) samples, (X = 0 – 4).

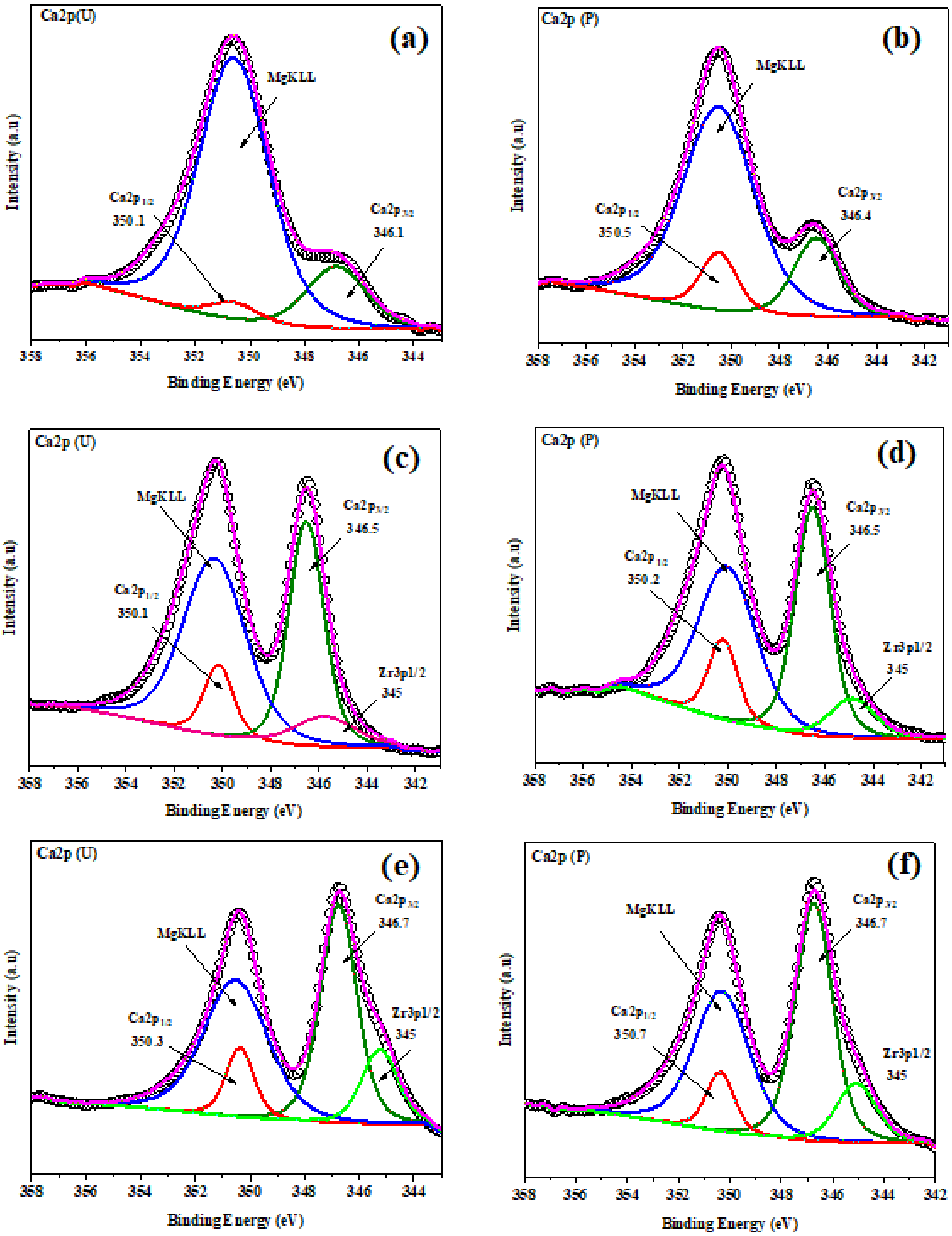
Ca2p(U)
(a)
MgKLL
$Ca2p_{1/2}$
350.1
$Ca2p_{3/2}$
346.1
Intensity (a.u)
Binding Energy (eV)
358 356 354 352 350 348 346 344
Ca2p (P)
(b)
MgKLL
$Ca2p_{1/2}$
350.5
$Ca2p_{3/2}$
346.4
Intensity (a.u)
Binding Energy (eV)
358 356 354 352 350 348 346 344 342
Ca2p (U)
(c)
MgKLL
$Ca2p_{1/2}$
350.1
$Ca2p_{3/2}$
346.5
Zr3p1/2
345
Intensity (a.u)
Binding Energy (eV)
358 356 354 352 350 348 346 344 342
Ca2p (P)
(d)
MgKLL
$Ca2p_{1/2}$
350.2
$Ca2p_{3/2}$
346.5
Zr3p1/2
345
Intensity (a.u)
Binding Energy (eV)
358 356 354 352 350 348 346 344 342
Ca2p (U)
(e)
MgKLL
$Ca2p_{1/2}$
350.3
$Ca2p_{3/2}$
346.7
Zr3p1/2
345
Intensity (a.u)
Binding Energy (eV)
358 356 354 352 350 348 346 344
Ca2p (P)
(f)
MgKLL
$Ca2p_{1/2}$
350.7
$Ca2p_{3/2}$
346.7
Zr3p1/2
345
Intensity (a.u)
Binding Energy (eV)
358 356 354 352 350 348 346 344 342

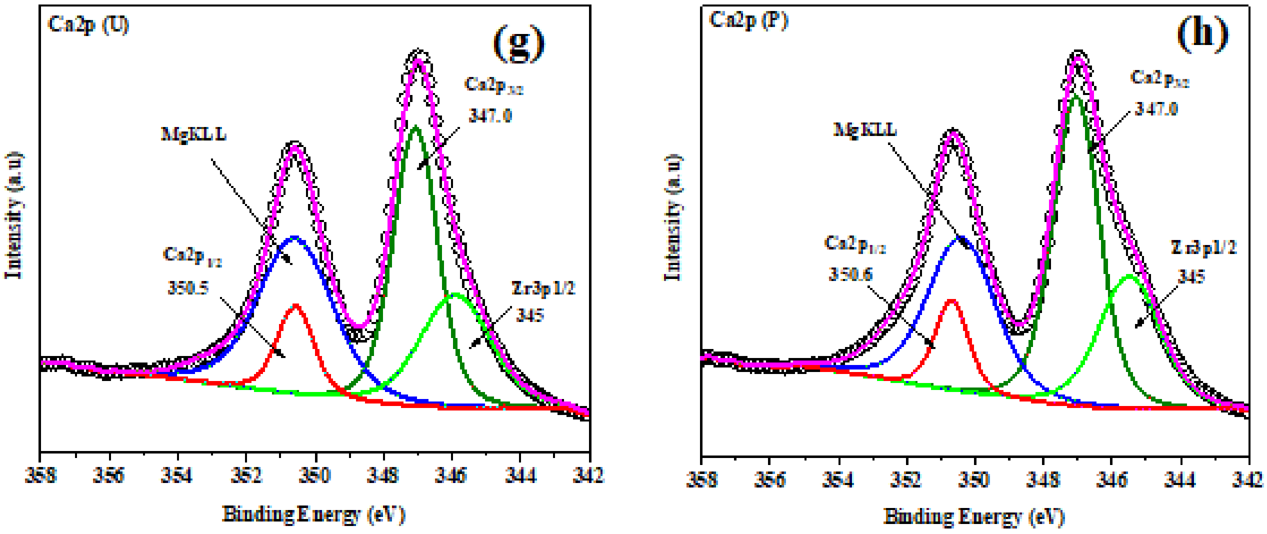

Figure 4.9. XPS spectra of both, uncharged and electret surfaces of MCSZO -X (X = 0 – 4) samples, i.e., (a, b) MCSZO-0, (c,d) MCSZO-1, (e, f) MCSZO-2, (g, h) MCSZO-3, and (i, j) MCSZO-4, for Ca 2p. Representation of Ca 2p spectra for uncharged MCSZO-X, (a, c, e, g) and electret of MCSZO-X, (b, d, f, h) samples (X = 0 – 4).

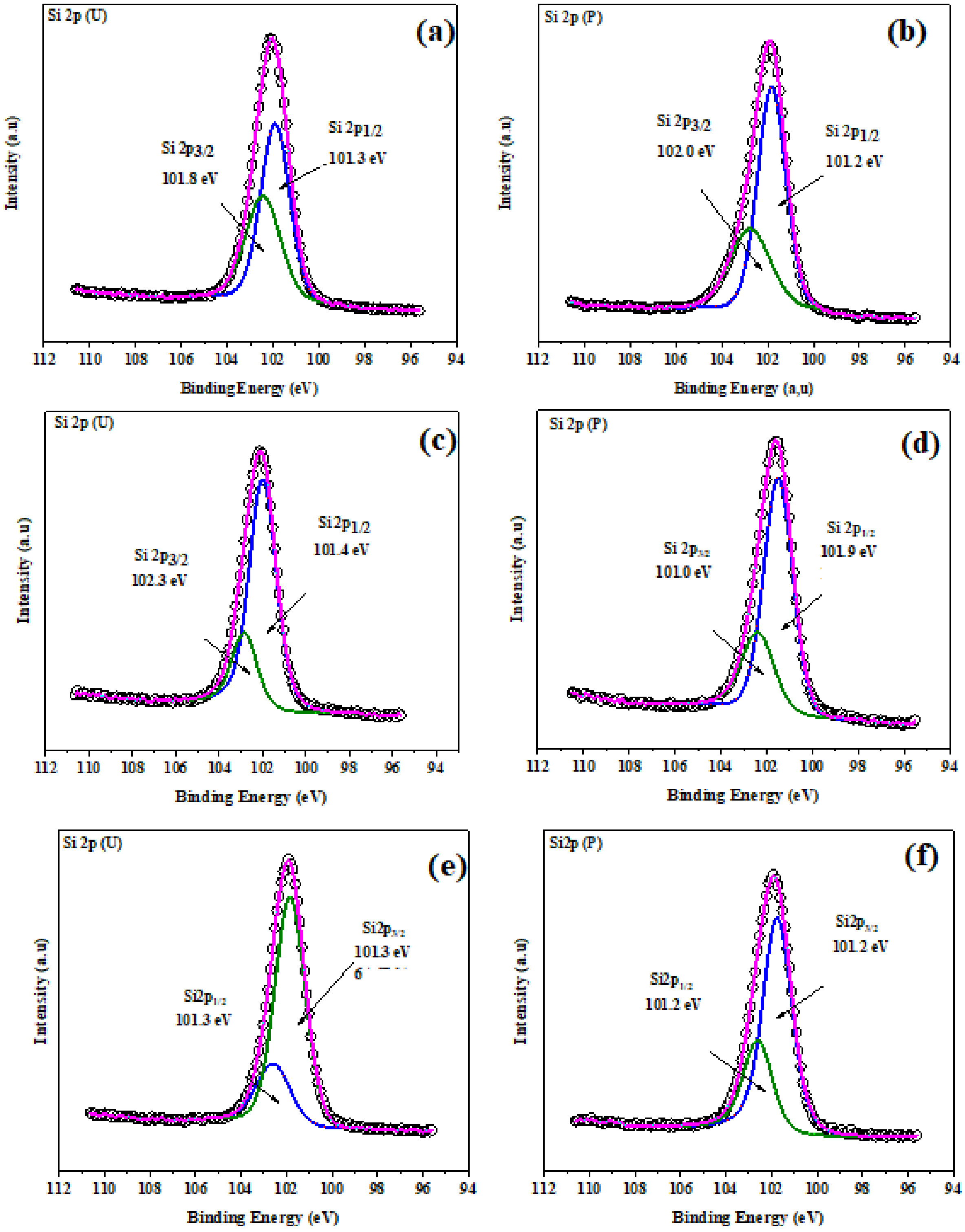
Si 2p (U)
(a)
Si 2p3/2
101.8 eV
Si 2p1/2
101.3 eV
Intensity (a.u)
112 110 108 106 104 102 100 98 96 94
Binding Energy (eV)
Si 2p (P)
(b)
Si 2p3/2
102.0 eV
Si 2p1/2
101.2 eV
Intensity (a.u)
112 110 108 106 104 102 100 98 96 94
Binding Energy (a,u)
Si 2p (U)
(c)
Si 2p3/2
102.3 eV
Si 2p1/2
101.4 eV
Intensity (a.u)
112 110 108 106 104 102 100 98 96 94
Binding Energy (eV)
Si 2p (P)
(d)
Si 2p3/2
101.0 eV
Si 2p1/2
101.9 eV
Intensity (a.u)
112 110 108 106 104 102 100 98 96 94
Binding Energy (eV)
Si 2p (U)
(e)
Si2p1/2
101.3 eV
Si2p3/2
101.3 eV
Intensity (a.u)
112 110 108 106 104 102 100 98 96 94
Binding Energy (eV)
Si2p (P)
(f)
Si2p1/2
101.2 eV
Si2p3/2
101.2 eV
Intensity (a.u)
112 110 108 106 104 102 100 98 96 94
Binding Energy (eV)

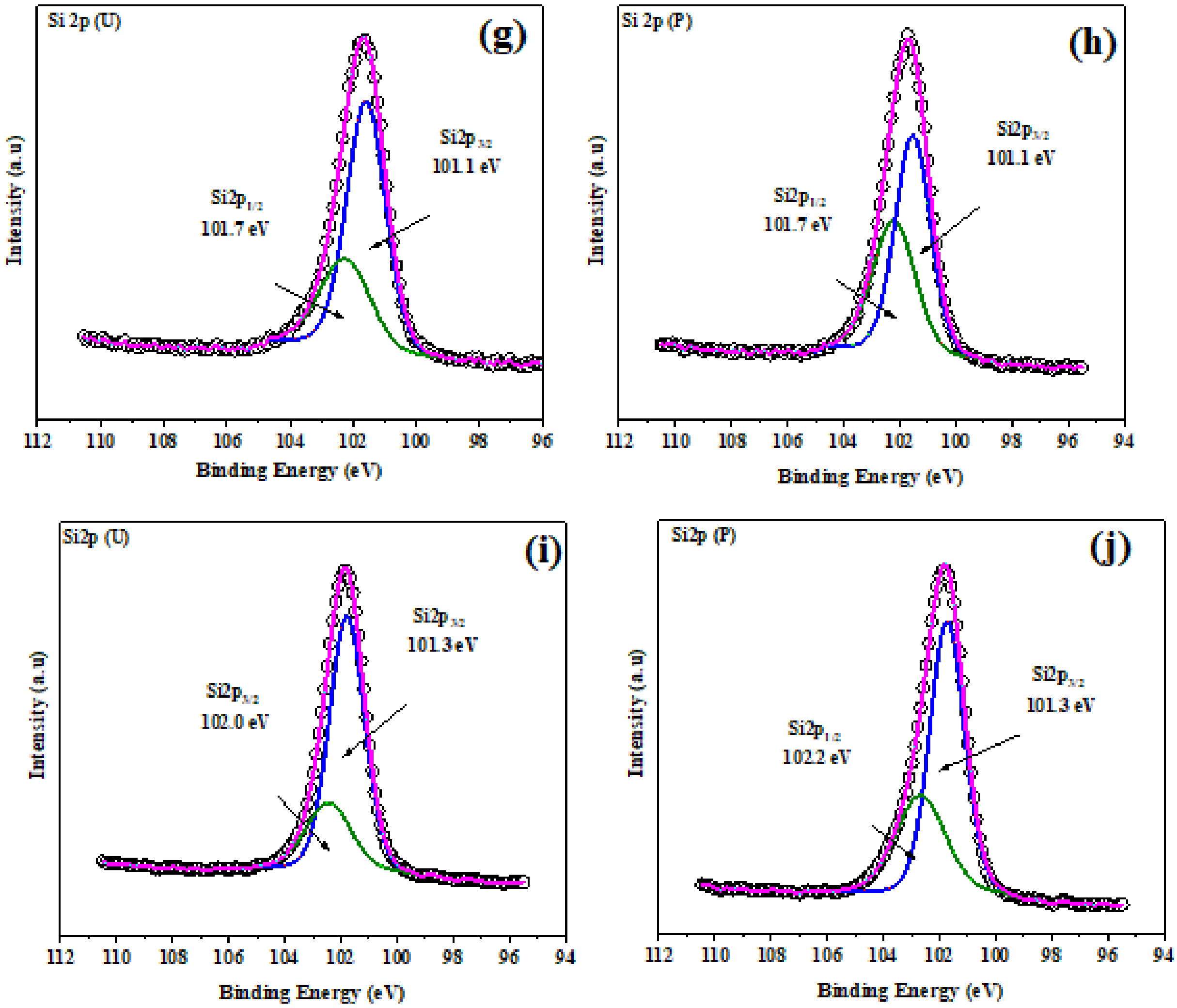

Figure 4.10. XPS spectra of both, uncharged and electret surfaces of MCSZO -X (X = 0 – 4) samples, i.e., (a, b) MCSZO-0, (c,d) MCSZO-1, (e, f) MCSZO-2, (g, h) MCSZO-3, and (i, j) MCSZO-4, for Si 2p. Representation of Si 2p spectra for uncharged MCSZO-X, (a, c, e, g, i) and electret of MCSZO-X, (b, d, f, h, j) samples, (X = 0 – 4).

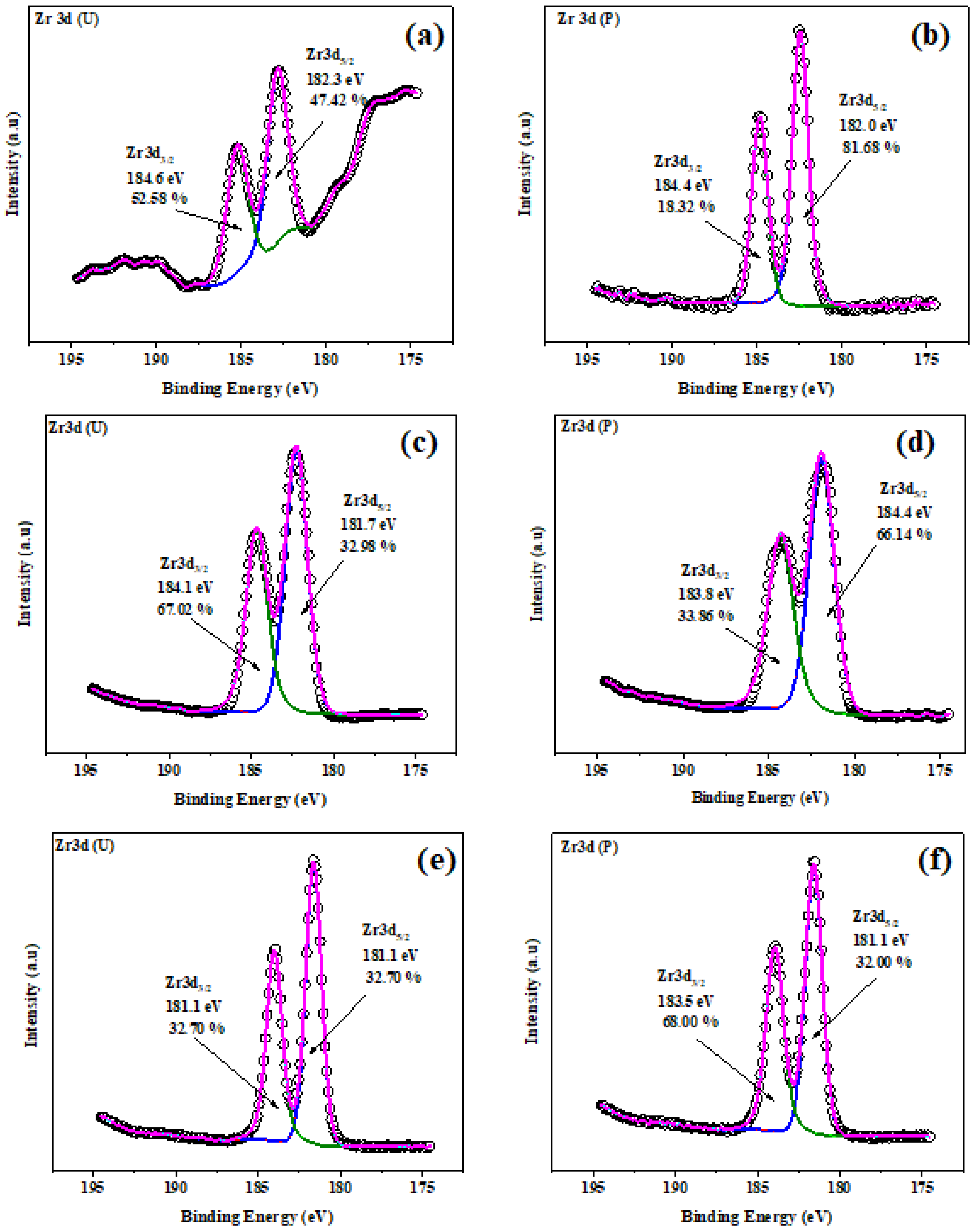
Zr 3d (U)
(a)
Zr3d5/2
182.3 eV
47.42 %
Zr3d3/2
184.6 eV
52.58 %
Intensity (a.u)
195
190
185
180
175
Binding Energy (eV)
Zr 3d (P)
(b)
Zr3d5/2
182.0 eV
81.68 %
Zr3d3/2
184.4 eV
18.32 %
Intensity (a.u)
195
190
185
180
175
Binding Energy (eV)
Zr3d (U)
(c)
Zr3d5/2
181.7 eV
32.98 %
Zr3d3/2
184.1 eV
67.02 %
Intensity (a.u)
195
190
185
180
175
Binding Energy (eV)
Zr3d (P)
(d)
Zr3d5/2
184.4 eV
66.14 %
Zr3d3/2
183.8 eV
33.86 %
Intensity (a.u)
195
190
185
180
175
Binding Energy (eV)
Zr3d (U)
(e)
Zr3d5/2
181.1 eV
32.70 %
Zr3d3/2
181.1 eV
32.70 %
Intensity (a.u)
195
190
185
180
175
Binding Energy (eV)
Zr3d (P)
(f)
Zr3d5/2
181.1 eV
32.00 %
Zr3d3/2
183.5 eV
68.00 %
Intensity (a.u)
195
190
185
180
175
Binding Energy (eV)

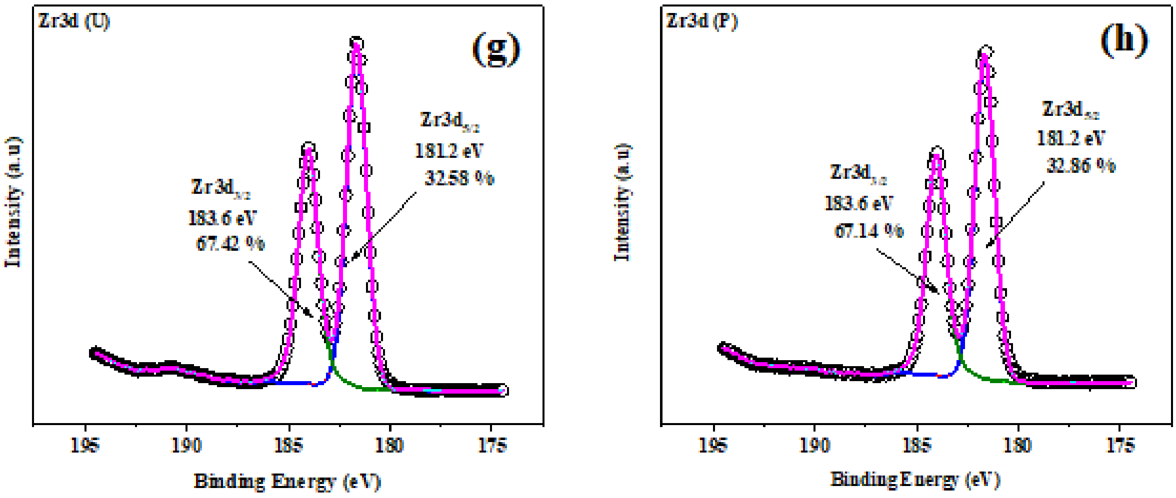

Figure 4.11. XPS spectra of both, uncharged and electret surfaces of MCSZO -X (X = 0 – 4) samples, i.e., (a, b) MCSZO-0, (c,d) MCSZO-1, (e, f) MCSZO-2, (g, h) MCSZO-3, and (i, j) MCSZO-4, for Zr 3d. Representation of Zr 3d spectra for uncharged MCSZO-X, (a, c, e, g) and electret of MCSZO-X, (b, d, f, h) samples (X = 0 – 4).

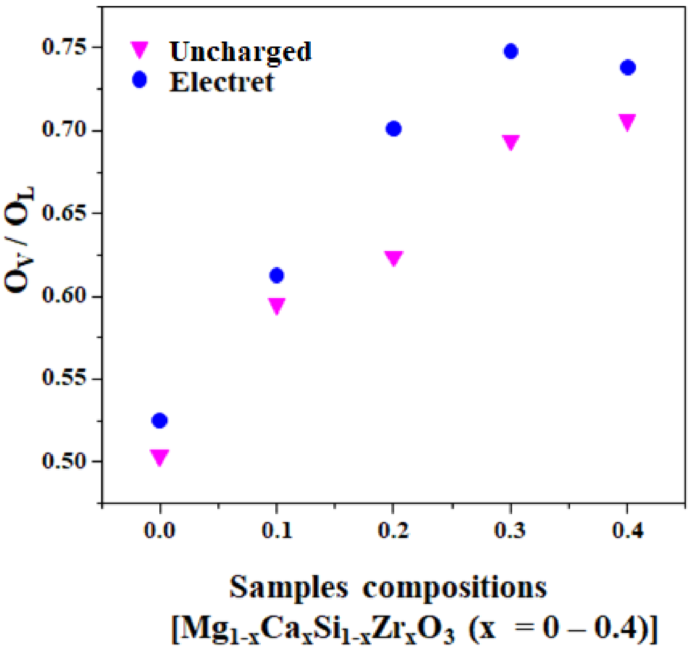

Figure 4.12. Variation in oxygen deficiencies on uncharged and electret surfaces of $Mg_{1-x}Ca_xSi_{1-x}Zr_xO_3$ *(x = 0, 0.1, 0.2, 0.3, 0.4, MCSZO-X) samples. The graph represents the increase in the oxygen deficiency in the electret samples with respect to their corresponding uncharged samples.*

4.5. Synergistic effect of electret and electrodynamic stimulation on cellular response

4.5.1. Cell viability

The cell viability increases with increase in the culture duration on both, uncharged and electret samples as well as electrodynamically treated (both, uncharged and electret) samples [Figure. 4.13 (a − c)]. Statistical analyses revealed that the **e**lectrodynamic field treated (both, uncharged and electret) samples show significantly higher cell viability in comparison to uncharged control [shown as (*) in [Figure. 4.13 (a−c)]. The viability of MG-63 cells on electret surfaces of MCSZO- X increased from 111, 117, 124, 158, 122% of uncharged HA to 126, 131, 136, 144, 134% of uncharged HA, respectively, with the increase in the incubation period from 5 to 7 days.

Furthermore, the negatively charged [MCSZO- X (N-MCSZO-X)] and positively charged [MCSZO-X (P-MCSZO-X)] electrets show significantly higher cell viability than the uncharged surface of MCSZO-X (U-MCSZO-X), after 5 and 7 days of incubation [shown as (@) in Figure. 4.13 (b, c)]. These results suggest that the electrets promote cell proliferation as compared to uncharged surface of samples. Also, the electrodynamic field treated positive [E(P)-MCSZO] and negative [E(N)-MCSZO] ends of electrets as well as the uncharged [U(E)-MCSZO] surfaces of MCSZO-X and HA samples represent the higher cell viability of osteoblast-like cells than untreated samples. However, the electrodynamic field treated negative end of electret of the MCSZO [E(N)-MCSZO] electrets represents higher cell viability than N-MCSZO and N-HA electret surfaces after incubation of 5 and 7 days [shown (@@) and (**) in Figure 4.13 (b, c)]. However, the electrodynamic field treated positive end of the E(P)-MCSZO electret, and E(P)-HA samples shows the significantly higher cell viability than P-MCSZO and P-HA samples [represents (***) and (@@@) in Figure. 4.13 (a, b, c)], respectively.

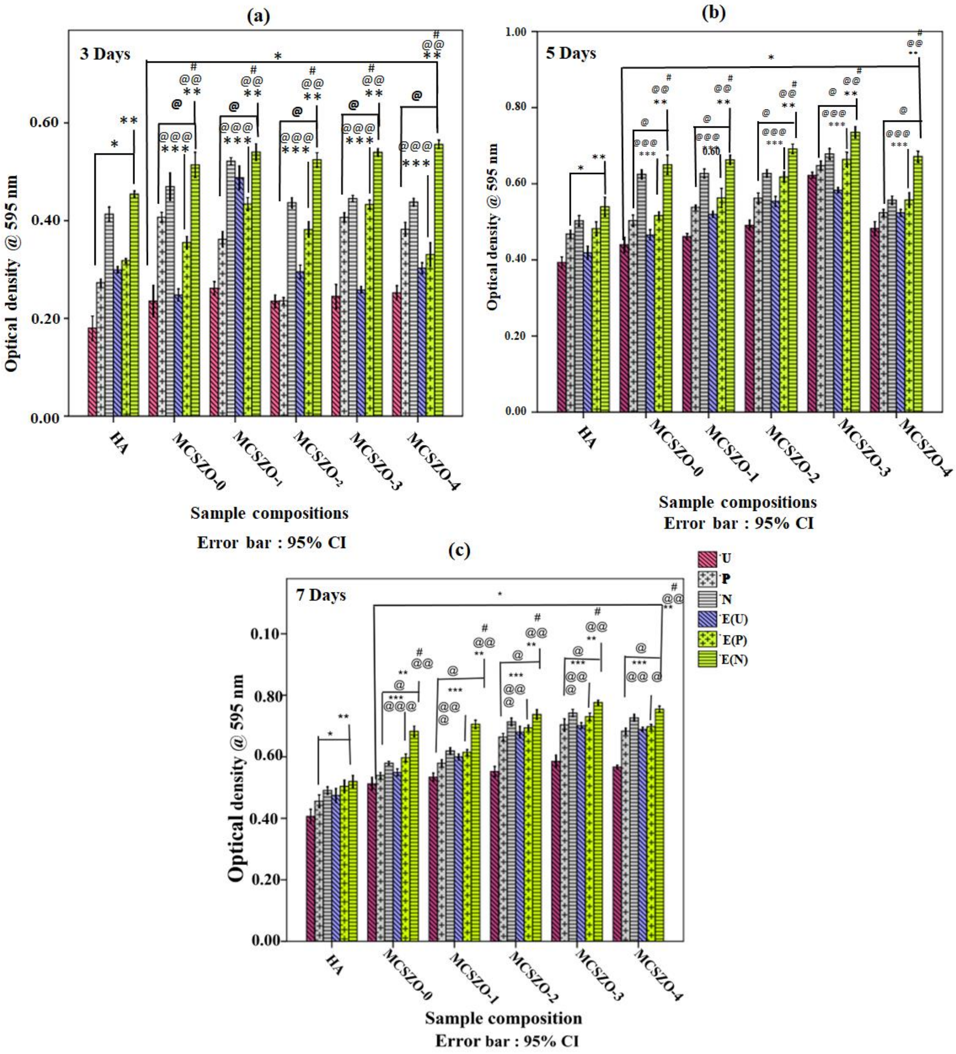

Figure 4.13. Viability of MG-63 cells on uncharged, electrets and electrodynamically treated electrets of MCSZO-X (X = 0 - 4) samples and HA control, after the culture duration of 3, 5, 7 days. (*) symbol denotes the significant variation for all uncharged, electrets and electrodynamically treated electrets of MCSZO-X samples and control in comparison to uncharged HA, at $p \leq 0.05$. The (@) symbol indicates a significant variation for all treated MCSZO-X samples with respect to their corresponding uncharged MCSZO-X samples, at $p \leq 0.05$. The (**) symbol indicates the significant variation for all negatively charged electrodynamic stimulated [E(N)] MCSZO-X electret samples and HA control in comparison to negatively charged electret [N] HA, at $p \leq 0.05$. The (@@) symbol indicates significant variation for all of the negatively charged electrodynamic stimulated [E(N)] MCSZO-X

electret samples with respect to their corresponding negatively charged [N] MCSZO-X electret samples, at $p \leq 0.05$. The (***) and (@@@) symbols indicates the significant variation for all of the positively charged electrodynamic stimulated [E(P)] MCSZO-X electret samples and HA control with respect to positive end of [P] HA electret and corresponding [P] MCSZO-X samples, respectively, at $p \leq 0.05$. (#) represents significant variation for all of the electrodynamically stimulated MCSZO-X electret samples with respect to their corresponding uncharged MCSZO samples and HA control, at $p \leq 0.05$. The U, P, N represents the uncharge, positive electret and negative electret, respectively.

Therefore, the MTT results reveal that synergistic action of electret and electrodynamic field treatment enhances the proliferation of MG-63 cells in comparison to mere electret samples. Overall, it has been observed that with the increase of the concentration of MCSZO-X, proliferation of MG-63 cells increases on the negative end of electret as well as electrodynamic field treated MCSZO-X samples. This shows that the electret and electrodynamic field stimulation accelerates cell adhesion (surface charge), proliferation (stimulating field) and growth (combined/synergistic of both).

4.5.2. Morphological analyses

The population of MG-63 cells was observed to increase with an increasing in the concentration of Ca and Zr from 0 to 0.3. Moreover, the negative end of electret samples represents higher cell density than the positive end of electret and the uncharged surfaces [Figure. 4.14]. Also, electrodynamic field treatment increases the cell density in all of the samples, as compared to untreated samples.

However, electrodynamic field treated negative end of electret samples show higher cell density than untreated samples. It has been observed that the electrodynamic field treated negative end of the electret of $Mg_{0.7}Ca_{0.3}Si_{0.7}Zr_{0.3}O_3$ (x = 0.3) show the maximum cell density [Figure. 4.14].

The electrodynamically stimulated negative end of the [E(N)-MCSZO] electret shows maximum cell density as compared to the positive end of the [E(P)-MCSZO] electret and [E(U)-MCSZO] uncharged surfaces. Overall, the results suggested that the combined action of the electret and electrodynamic simulation demonstrates the accelerated proliferation of MG-63 cells for the similar incubation period.

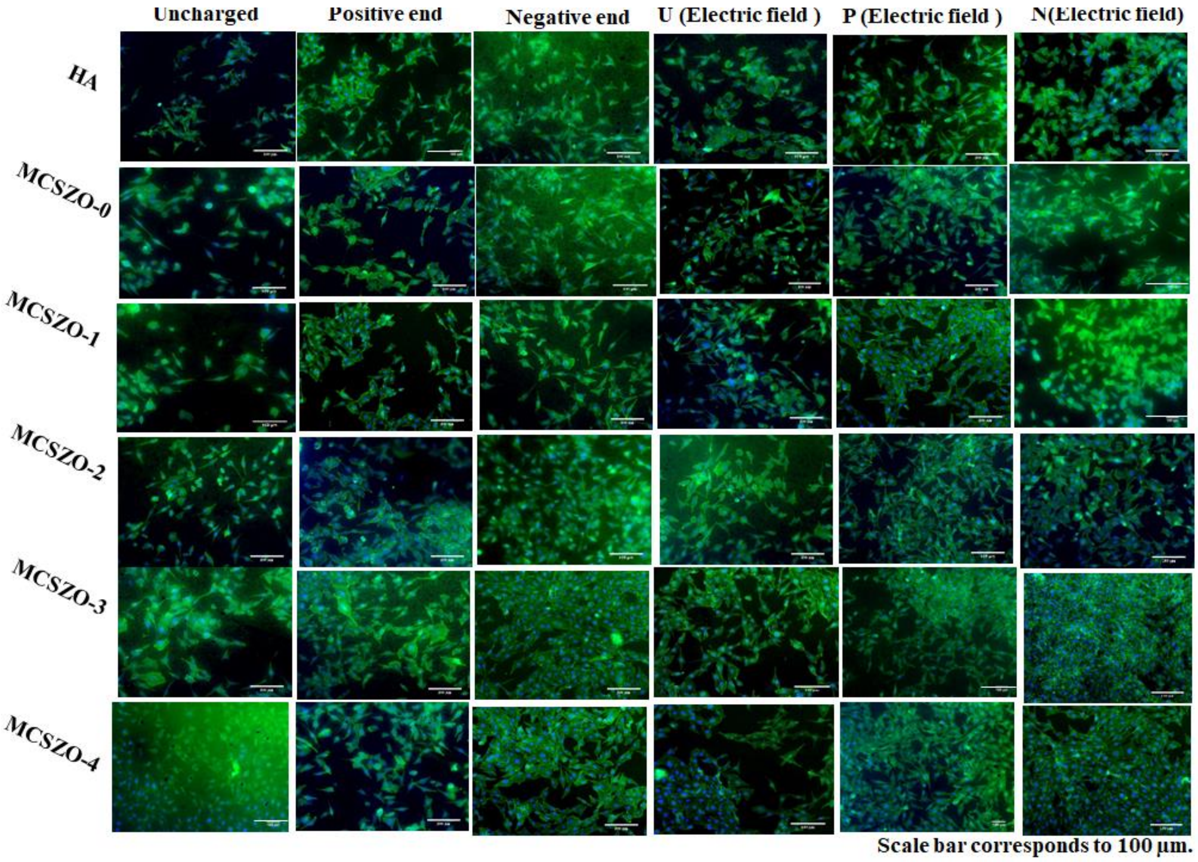

Figure 4.14. Morphological analyses of osteoblast-like MG-63 cells, cultured on uncharged and electrodynamically stimulated MCSZO -X (X = 0 - 4) electrets as well as HA samples using fluorescence microscopy. The U, P and N represent the uncharged, positive electret and negative electret of MCSZO-X and HA samples. The electrodynamic stimulation treated uncharged, positively and negatively charged electrets are denoted as U(E), P(E) and N(E), respectively.

4.5.3. Alkaline phosphatase (ALP) activity

Figure. 4.15 shows ALP activity of osteoblast-like cells on uncharged, electrets and electrodynamically treated electret samples and HA control. After 7 days of incubation, all of the untreated and treated samples (apart from uncharged MCSZO-X) demonstrate considerably higher ALP activity than the untreated and electrodynamically treated HA [Figure. 4.15a]. However, all the electrodynamic field treated electret samples show a significant increase in ALP activity in comparison with untreated samples and HA, after 14 days [Figure. 4.15b]. This study demonstrates that the negative end of electret samples show significant increase in ALP activity than the positive end of electrets and uncharged surfaces. The electrodynamic stimulation treated electret surfaces further increased the ALP activity, which led to remarkable rise in the level of ALP activity with respect to their corresponding electret samples, which were cultured without electrodynamic stimulation [Figure. 4.15 (a, b)]. Out of all the treated and untreated samples, the electrodynamically stimulated negative end of electret samples has the highest levels of ALP activity. This finding demonstrates that the combined action of electret formation and electrodynamic stimulation facilitates the earlier differentiation of MG-63 cells. The ALP activity on the negative end of electret and the electrodynamically treated negative end of electret of MCSZO - X samples are measured to be 2.04, 3.08, 3.41, 3.67, 3.59 times of uncharged HA and 2.21, 3.47, 4.15, 4.42, 4.33 times of uncharged HA, respectively, after 14 days. It is clear from the above results that the electrodynamic stimulation treated negative end of the MSCZO - X electret (X = 3 and 4) samples considerably promote osteogenic differentiation as compared to the electrodynamically treated negative end of MCSZO-X (X = 0, 1 and 2) electret samples.

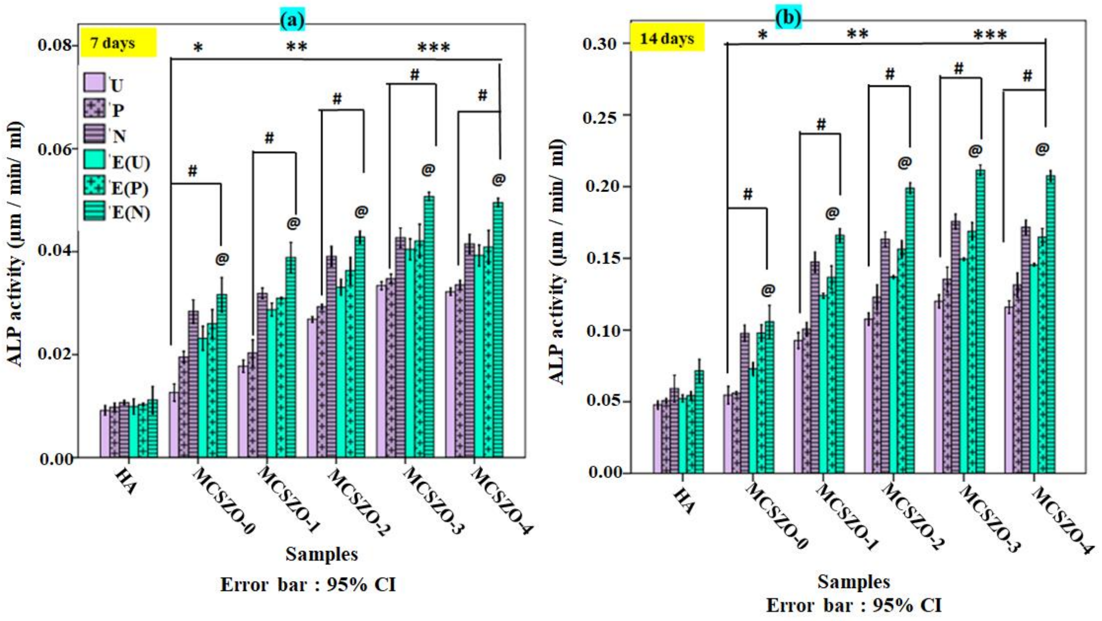

Figure 4.15. Alkaline phosphatase (ALP) activity of osteoblast-like MG-63 cells, seeded on uncharged and electrodynamically stimulated MCSZO -X (X = 0 - 4) electret samples and HA control, after the culture duration of (a) 7 and (b) 14 days. [U-uncharged, P- positive electret, and N-negative electret. The electrodynamic stimulation treated uncharged, positively and negatively charged electrets are denoted as U(E), P(E) and N(E), respectively.]. The symbols (*), (**), and (***) denote the significant variation, at $p \leq 0.05$ *in the mean values of ALP activity between the untreated and treated MCSZO-X samples as compared to U, P and E (P) HA samples, respectively. The (#) denotes the significant variation, at* $p \leq 0.05$ *in the mean values of ALP activity between the electrodynamic simulation treated and untreated MCSZO-X electret samples as compared to uncharged MCSZO-X samples, at* $p \leq 0.05$*. (@) symbol represents the significant variation, among the mean values of ALP activity on negatively charged electrodynamic stimulated E(N) MCSZO-X electret samples in comparison to their respective negatively electret samples, at* $p \leq 0.05$*.*

4.5.4. Concentration of intracellular Ca^{2+} ions

The level of intracellular Ca^{2+} was measured using MG-63 cells, loaded with the Fura-2 AM (intracellular Ca^{2+} fluorescence indicator) on uncharged, electrets and electrodynamically treated electret samples and HA control, which is expressed in terms of the ratio of mean values of peak fluorescence intensity at 380 and 340 nm [Figure. 4.16]. The cells, adhered on the uncharged and electret samples show comparatively higher concentration of intracellular Ca^{2+} under the application of electrodynamic treatment in comparison to nontreated as well as treated HA control [Figure. 4.16]. Additionally, as compared to the MCSZO-X samples, all the negative end of electrets (N-MCSZO-X) and electrodynamically treated (E-U-MCSZO-X, E-P-MCSZO-X and E-N-MCSZO-X) samples have shown a considerable increase in the amount of Ca^{2+} [Figure. 4.16]. The level of intracellular Ca^{2+} at the negative end of electret and all electrodynamic stimulation treated (E-U-MCSZO-X, E-P-MCSZO-X and E-N-MCSZO-X) MCSZO-X samples are measured to be 1.8, 2.7, 3.0, 3.0, 3.0 times that of uncharged HA, 1.9, 2.5, 2.8, 2.9, 2.9 times that uncharged HA, 1.9, 2.8, 2.9, 3.1, 3.0 times that of uncharged HA and 2.2, 3.3, 3.5, 3.9, 3.8 times that of uncharged HA, respectively. Overall, electret and electrodynamic stimulation synergistically increase the Ca^{2+} concentration in the osteoblast-like cells, which positively influences the osteoblastic functionality, especially those, cultured on electrodynamic stimulated negative end of MCSZO-X electrets.

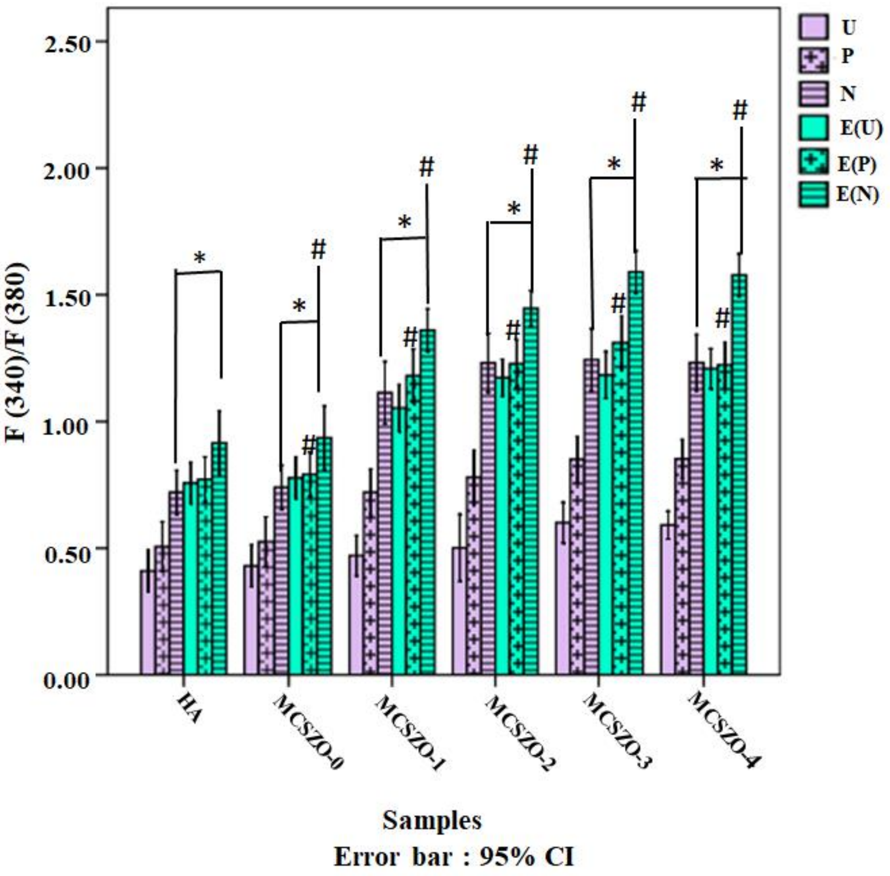

Figure 4.16. Intracellular Ca^{2+} *concentration in MG-63 cells, seeded on uncharged and electrodynamically stimulated MCSZO -X (X = 0 - 4) electret samples and HA control. The graph demonstrates the ratios of the mean values of the peak fluorescence intensity, recorded at the excitation of 340 and 380 nm, for Fura-2 AM (Intracellular* Ca^{2+} *indicator) loaded MG-63 cells, cultured on uncharged and electrodynamically stimulated MCSZO -X (X = 0 - 4) electrets as well as HA samples. The asterisk (*) denotes a significant difference, among the mean peak value of estimated ratios for MG-63 cells, seeded on N, E (U), E (P) and E (N) MCSZO-X as well as HA control, as compared to uncharged and P HA, at* $p \leq 0.05$. *(#) mark represents the significant difference, at* $p \leq 0.05$, *among the mean peak value of estimated ratios for MG-63 cells, cultured on electrodynamic stimulated uncharged / electret MCSZO-X samples as compared to the estimated mean peak values for their corresponding*

uncharged/electret MCSZO-X samples, cultured in absence of electrodynamic field, at $p \leq 0.05$. *The U, P, N represents the charge, positive electret and negative electret, respectively.*

4.6. Discussion

In the present study, the successful doping of higher ionic radius Ca (1.34 Å) at the Mg (0.72 Å) site having smaller ionic radius and higher ionic radius Zr (0.74 Å) ion at the Si (0.42 Å) site having smaller ionic radius was confirmed by the phase analyses [Figure. 4.1]. It was observed that the peak position shifted towards lower 2θ values on increasing the concentration of Ca and Zr from 0 to 3. This is due to the lattice expansion that occurred within $MgSiO_3$. However, as the value of x increases from 0.3 to 0.4, the peak slightly shifts towards the higher angle. On increasing the concentration of Ca and Zr from 0.3 to 0.4, minor phases ($CaSiO_3$, Ca_2MgSiO_7, Mg_2SiO_4 and $CaMg(SiO_3)_2$ started to form.

Overall, the results reveal that the negative end of Ca and Zr codoped MCSZO-X electret samples accelerates cell adhesion, proliferation, and differentiation in response to electrodynamic stimulation treatment [Figures. 4.13, 4.14 and 4.15]. In DI water and culture media, the contact angle decreases from 45.5° to 25.6° and 40.1° to 25.1° with increase of the concentration of Ca and Zr from 0.1 to 0.4, respectively, on negative end of electrets as compared to the respective positive end of electrets, uncharged MCSZO-X and HA samples [Figures. 4.5 (a, b)]. Consequently, higher hydrophilicity was observed for negative end of MCSZO-X (X = 0.3) electrets.

Additionally, XPS analyses reveal that the oxygen deficiency ($Mg_{1-x}Ca_xSi_{1-x}Zr_xO_{3-\delta}$) increased from 0.18 to 0.36 with the increase of the concentration of Ca and Zr from 0.1 to 0.4 in $MgSiO_3$. The formation of electrets also favours the generation of oxygen vacancies to produce active sites for the adhesion of water, which increases the surface hydrophilicity [Figure. 4.5]. Such enhancement in hydrophilicity on the negative end of electrets accelerates the cellular response [40-42] [38-41].

The negative end of electrets operates as a stimulus for the adhesion and proliferation of cells by attracting Ca^{2+}, H^{+} ions from culture media, which further facilitate the adhesion of fibronectin and integrin proteins [Figure 4.17 (a)] [43, 44]. Further, the application of electric field stimulation trigger the voltage-gated Ca^{2+} channels in the cell membrane as well as regulate the configuration of receptors, present in the endoplasmic reticulum [Figure 4.17 (b)] [43, 45]. As a result, the local electric field makes it easier for Ca^{2+} ions to enter into the cell from the endoplasmic reticulum and extracellular milieu [43, 45]. This increased amount of intracellular Ca^{2+} ions helps in the production of transforming growth factor and bone morphogenic protein-2, which is crucial for regulation of cellular metabolism [Figure 4.17] [42, 43, 45-47].

Therefore, the combined action of electrodynamical stimulation and the negative end of electret accelerates cellular adhesion, proliferation, and differentiation. Overall, the XPS analyses as well as contact angle measurement results reveal that the negative end of MCSZO- X electret samples leads to increased hydrophilicity, resulting in improved cellular responsiveness [44, 48-50].

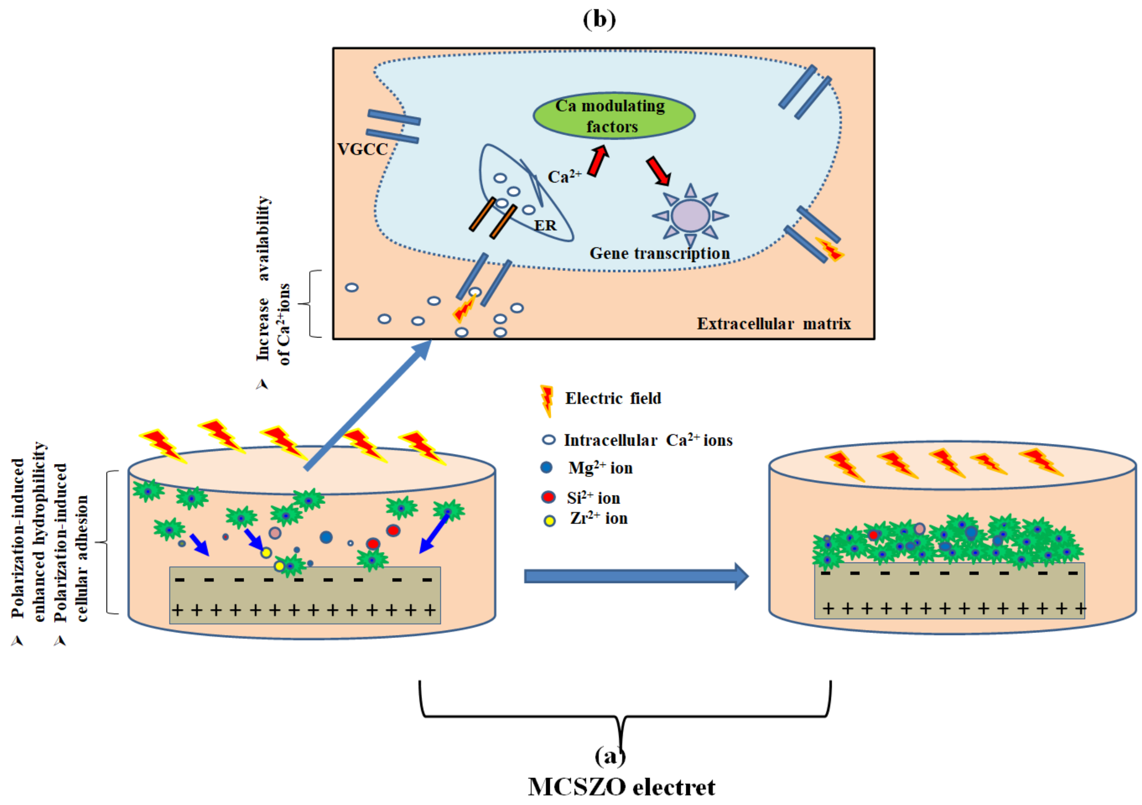

Figure 4.17 schematic diagram demonstrating the Synergistic effect of electrostatic and electrodynamic electrical stimulation on osteogenic responses of MCSZO-X (X= 0 - 4). (a) The negative end of electret operates as a stimulus for the adhesion and proliferation of cells by attracting Ca2+, H+ ions from culture media which further attract negatively charged fibronectin and integrin protein. Also, the negative end of MCSZO-X (X = 0 - 4) electrets exhibit noticeable increase in surface hydrophilicity. (b) Further, the application of electric field stimulation triggers the voltage-gated Ca^{2+} channels located on the cell membrane as well as also regulate the configuration of receptors present in endoplasmic reticulum. The local electric field makes it easier for Ca^{2+} ions to enter into the cell from the endoplasmic reticulum and extracellular milieu. This increased amount of intracellular Ca^{2+} ions helps in the production of transforming growth factor and bone morphogenic protein-2, which is crucial for regulation of cellular metabolism.

In comparison to pure $MgSiO_3$ and doped (X = 1 and 2) MCSZO-X samples, the higher amount of Ca (X = 3) and Zr (X = 3) doped $MgSiO_3$ samples demonstrates a notably higher propensity for the adhesion and growth of both MG-63 cells, which is discussed in section 4.5. The ion leching analyses suggest that the compositions, X = 0, X = 1 and X= 2 leached significantly higher amounts of Mg^{2+} and Si^{4+} than compositions, X = 3 and X = 4, for both, electrets and uncharged samples. However, with the increase in the content of Ca and Zr in $MgSiO_3$, the amount of leached Ca^{2+} and Zr^{4+} into the SBF increases with the soaking period for both, electrets and uncharged samples [Figures. 4.4 (c, d)]. Mg^{2+}, Ca^{2+}, Zr^{4+}, and Si^{4+} ions accelerate cellular adhesion, proliferation and bone formation [3]. Particularly, the presence of Si^{4+} ions in $Si(OH)_4$ facilitate the interaction with Ca^{2+} and PO_4^{3-}, present in SBF, which lead to formation of HA i.e., mineralization [51-53].

Moreover, the concentrations of (2 - 4 mmol) of Ca^{2+} is favourable for proliferation and differentiation of osteoblasts, which promotes the osteogenic response [54]. In the present study, MCSZO-X (X = 3 and 4) samples show augmented Ca^{2+} dissolution in SBF [Figure. 4.4] which help in increasing the availability of Ca^{2+} ions in the extracellular matrix that improve the proliferation [51, 55]. It can be another reason for increasing the intercellular Ca^{2+} ions for these samples which consequently, results in enhanced osteogenic response [Figures. 4.14, 4.15 and 4.16].

As a result, the combined action of electrostatic, electrodynamic stimulated electret and Ca and Zr co-doping in $MgSiO_3$ bioceramics offers a potential way to improve the osteogenic response of MCSZO-X bioceramics.

4.7. Closure

In recent study, pure and Ca/Zr co-doped MCSZO-X bioceramics were prepared using solid-state synthesis method, followed by sintering at optimal temperatures of 1380, 1350 and 1320° C for 3 h.

The influence of co- substitution of Ca and Zr in MCSZO-X was studied in terms of sinterability /densification, microstructure, ion dissolution and biocompatibility. The consolidation temperatures of MCSZO-X bioceramics were reduced from 1380 to 1320 with substitution of Ca^{2+} and Zr^{4+} from 0.1 to 0.4. The successful doping of higher ionic radius Ca at the Mg site having smaller ionic radius and higher ionic radius Zr ion at the Si site having smaller ionic radius was confirmed by phase analyses. The microstructural analyses reveal that with increase in the contents of Ca^{2+} and Zr^{4+} in MCSZO-X samples, the grain size of MCSZO-X ceramics increases from 1.69 ± 0.25 to 2.18 ± 0.43 µm.

ICP-AES measurements demonstrate that with the increase of the content of Ca and Zr from X = 0 -4 in MCSZO-X samples, the amount of leached Ca^{2+} and Zr^{4+} into the SBF increases with the soaking period for both, electrets and uncharged samples. In DI water and culture media, the contact angle decreases from 45.5° to 25.6° and 40.1° to 25.1°, respectively, with the increase of the concentration of Ca and Zr from 0.1 to 0.4, respectively, on the negative end of electret as compared to their respective positive end of electrets and uncharged MCSZO-X samples. Consequently, higher hydrophilicity was observed for the negative end of MCSZO-X electrets.

Furthermore, MG-63 cells, cultured on Ca^{2+} and Zr^{4+} doped MCSZO-X (X = 0 - 4) demonstrated an increase in the cellular response (cell differentiation, proliferation and cell adhesion), with the increase in the concentration of Ca and Zr from 0.1 to 0.4. Moreover, a better osteogenic response was observed for higher concentrations of Ca (0.3 and 0.4) and Zr (0.3 and 0.4) doping in $MgSiO_3$ bioelectrets. In addition, electrostatic and electrodynamic simulation further improved the cellular response on the negative end of Ca and Zr doped MCSZO-X electret samples, which is attributed to the induced metabolic signalling passageways of the cells, as demonstrated by intracellular Ca^{2+} ion measurements.

Particularly, the increase in the level of intracellular Ca^{2+} ions indicate the activation of calcium modifying factors with the application of electric field, which subsequently, regulates cellular metabolism. Overall, the electrostatic and electrodynamic electric field stimulated Ca^{2+} and Zr^{4+} doped MCSZO-X samples exhibit the excellent osteogenic properties and potential for orthopedic implant application.

Bibliography

[1] Song M E, Kim J S, Joung M R, Nahm S, Kim Y S, Paik J H and Choi B H 2008 Synthesis and microwave dielectric properties of MgSiO3 ceramics *Journal of the American ceramic Society* **91** 2747-50

[2] Kanzaki M and Xue X 2017 Protoenstatite in MgSiO3 samples prepared by conventional solid state reaction *Journal of Mineralogical and Petrological Sciences* 170616

[3] Singh P, Yu X, Kumar A and Dubey A K 2022 Recent advances in silicate-based crystalline bioceramics for orthopedic applications: a review *Journal of Materials Science* 1-43

[4] Verma A S, Sharma A, Kumar A, Mukhopadhyay A, Kumar D and Dubey A K 2020 Multifunctional response of piezoelectric sodium potassium niobate (NKN)-toughened hydroxyapatite-based biocomposites *ACS Applied Bio Materials* **3** 5287-99

[5] Smyth J R 1974 Experimental study on the polymorphism of enstatite *American Mineralogist: Journal of Earth and Planetary Materials* **59** 345-52

[6] Mielcarek W, Nowak-Woźny D and Prociów K 2004 Correlation Between MgSiO3 Phases and Mechanical Durability of Steatite Ceramics *Journal of the European Ceramic Society* **24** 3817-21

[7] Parthasarathy S and Parthasarathi V 1976 A statistical study on the measurability of Bijvoet differences in crystals with type-I and type-II degree of centrosymmetry *Acta Crystallographica Section A: Crystal Physics, Diffraction, Theoretical and General Crystallography* **32** 768-71

[8] Shannon R D 1976 Revised effective ionic radii and systematic studies of interatomic distances in halides and chalcogenides *Acta crystallographica section A: crystal physics, diffraction, theoretical and general crystallography* **32** 751-67

[9] Sun H, Zhang Q, Yang H and Zou J 2007 (Ca1− xMgx) SiO3: a low-permittivity microwave dielectric ceramic system *Materials Science and Engineering: B* **138** 46-50

[10] Hameed I, Li L, Liu X Q and Chen X M 2022 Ultra low loss (Mg1− xCax) 2SiO4 dielectric ceramics (x= 0 to 0.15) for millimeter wave applications *Journal of the American Ceramic Society* **105** 2010-9

[11] Hazzez M, Ihzaz N, Boudard M and Oumezzine M 2016 Crystal structure, phase transitions, and magnetic properties of titanium doped La0. 5Sr0. 5MnO3 perovskites *Physica B: Condensed Matter* **487** 78-84

[12] Bian R, An S, Wang X, Xue Y, Tian J, Liang Z and Song Z 2023 Ca2+ doped TiO2 nano-sized polygon plates with oxygen vacancies for photocatalytic hydrogen evolution *International Journal of Hydrogen Energy*

[13] Ullah A, Liu H, Pengcheng Z, Hao H, Iqbal J, Cao M, Yao Z, Ahmad A S and Manan A 2019 Influence of Co substitution on the phase, microstructure, and microwave dielectric properties of MgSiO 3 ceramics *Journal of Materials Science: Materials in Electronics* **30** 6469-74

[14] Ullah A, Liu H, Hao H, Iqbal J, Yao Z, Cao M and Xu Q 2016 Phase and Microstructure Evaluation and Microwave Dielectric Properties of Mg1− x Ni x SiO3 Ceramics *Journal of Electronic Materials* **45** 5133-9

[15] Zhang H, Li N, Li K and Xue D 2007 Structural stability and formability of ABO3-type perovskite compounds *Acta Crystallographica Section B: Structural Science* **63** 812-8

[16] Oh T 2010 Comparison Between SiOC Thin Film by Plasma Enhance Chemical Vapor Deposition and SiO2 Thin Film by Fourier Transform Infrared Spectroscopy *Journal of The Korean Physical Society - J KOREAN PHYS SOC* **56**

[17] Vancea C, Mihailescu M, Adina N, Mosoarca G, Mihaela C, Duteanu N, Negrea P and Vasile M 2020 Batch and Fixed-Bed Column Studies on Palladium Recovery from Acidic Solution by Modified MgSiO3 *International Journal of Environmental Research and Public Health* **17** 9500

[18] Ernawati L, Wahyuono R A, Laksono A D, Ningrum A, Handayani K and Sabrina A 2021 Wollastonite (CaSiO3)-based Composite Particles for Synthetic Food Dyes (Brilliant Blue) Removal in Aquatic Media: Synthesis, Characterization and Kinetic study. In: *IOP Conference Series: Materials Science and Engineering*: IOP Publishing) p 012001

[19] Ernawati L, Yusariarta A, Alviany R and Halim A 2022 Effect of CaO/SiO2 compositions on the structure formation of mesoporous calcium silicate (CaSiO3) composite particles as adsorbent for organic dye removal. In: *IOP Conference Series: Earth and Environmental Science*: IOP Publishing) p 012008

[20] Sembiring S, Riyanto A, Simanjuntak W and Situmeang R 2017 Effect of MgO-SiO2 Ratio on the Forsterite (Mg2SiO4)) Precursors Characteristics Derived from Amorphous Rice Husk Silica *Oriental Journal of Chemistry* **33** 1828-36

[21] Prasanth C, Kumar H P, Pazhani R, Solomon S and Thomas J 2008 Synthesis, characterization and microwave dielectric properties of nanocrystalline CaZrO3 ceramics *Journal of alloys and compounds* **464** 306-9

[22] Evangeline B, Azeem P A, Rao R P, Swati G and Haranath D 2017 Structural and luminescent features of cerium doped CaZrO3 blue nanophosphors *Journal of Alloys and Compounds* **705** 618-23

[23] Terzioğlu P and Yucel S 2012 Synthesis of magnesium silicate from wheat husk ash: Effects of parameters on structural and surface properties *BioResources* **7**

[24] Shuai C, Mao Z, Han Z, Peng S and Li Z 2014 Fabrication and characterization of calcium silicate scaffolds for tissue engineering *Journal of Mechanics in Medicine and Biology* **14** 1450049

[25] Myat-Htun M, Noor A-F M, Kawashita M and Ismail Y M B 2022 Tailoring mechanical and in vitro biological properties of calcium–silicate based bioceramic through iron doping in developing future material *journal of the mechanical behavior of biomedical materials* **128** 105122

[26] Cheng Z and Teoh S-H 2004 Surface modification of ultra thin poly (ε-caprolactone) films using acrylic acid and collagen *Biomaterials* **25** 1991-2001

[27] Yang J, Bei J and Wang S 2002 Enhanced cell affinity of poly (D, L-lactide) by combining plasma treatment with collagen anchorage *Biomaterials* **23** 2607-14

[28] Cao H, Huo W, Ma S, Zhang Y and Zhou L 2018 Microstructure and Corrosion Behavior of Composite Coating on Pure Mg Acquired by Sliding Friction Treatment and Micro-Arc Oxidation. In: *Materials,*

[29] Greczynski G and Hultman L 2022 A step-by-step guide to perform x-ray photoelectron spectroscopy *Journal of Applied Physics* **132** 011101

[30] Zhu B, Liu B, Qu C, Zhang H, Guo W, Liang Z, Chen F and Zou R 2017 Tailoring Biomass-Derived Carbon for High-Performance Supercapacitor from Controllably Cultivated Algae Microspheres *Journal of Materials Chemistry A* **6**

[31] Dwivedi G, Joshi A G, Kumar S, Chou H, Yang K, Jhong D, Chan W, Ghosh A and Chatterjee S 2016 Electronic structure study of wide band gap magnetic semiconductor (La0. 6Pr0. 4) 0.65 Ca0. 35MnO3 nanocrystals in paramagnetic and ferromagnetic phases *Applied Physics Letters* **108** 172402

[32] Yuan Y, Zhao Z, Zheng J, Yang M, Qiu L, Li Z and Zou Z 2010 Polymerizable complex synthesis of BaZr 1− x Sn x O 3 photocatalysts: Role of Sn4+ in the band

structure and their photocatalytic water splitting activities *Journal of Materials Chemistry* **20** 6772-9

[33] Pilli A, Jones J, Chugh N, Kelber J, Pasquale F and LaVoie A 2019 Atomic layer deposition of BN as a novel capping barrier for B2O3 *Journal of Vacuum Science & Technology A: Vacuum, Surfaces, and Films* **37** 041505

[34] Wu Y, Lin Y and Xu J 2019 Synthesis of Ag–Ho, Ag–Sm, Ag–Zn, Ag–Cu, Ag–Cs, Ag–Zr, Ag–Er, Ag–Y and Ag–Co metal organic nanoparticles for UV-Vis-NIR wide-range bio-tissue imaging *Photochemical & Photobiological Sciences* **18** 1081-91

[35] Chen X, Liu L, Yu P Y and Mao S S 2011 Increasing Solar Absorption for Photocatalysis with Black Hydrogenated Titanium Dioxide Nanocrystals *Science* **331** 746-50

[36] Chastain J and King Jr R C 1992 Handbook of X-ray photoelectron spectroscopy *Perkin-Elmer Corporation* **40** 221

[37] Wegmann M, Watson L and Hendry A 2004 XPS Analysis of Submicrometer Barium Titanate Powder *Journal of the American Ceramic Society* **87** 371-7

[38] Schaub R, Thostrup P, Lopez N, Lægsgaard E, Stensgaard I, Nørskov J K and Besenbacher F 2001 Oxygen vacancies as active sites for water dissociation on rutile TiO 2 (110) *Physical Review Letters* **87** 266104

[39] Hu H, Ji H-F and Sun Y 2013 The effect of oxygen vacancies on water wettability of a ZnO surface *Physical Chemistry Chemical Physics* **15** 16557-65

[40] Yu H, Li J, Zhang Y, Yang S, Han K, Dong F, Ma T and Huang H 2019 Three-in-one oxygen vacancies: whole visible-spectrum absorption, efficient charge separation, and surface site activation for robust CO2 photoreduction *Angewandte Chemie International Edition* **58** 3880-4

[41] Wan L, Tian W, Li N, Chen D, Xu Q, Li H, He J and Lu J 2022 Hydrophilic porous PVDF membrane embedded with BaTiO3 featuring controlled oxygen vacancies for piezocatalytic water cleaning *Nano Energy* **94** 106930

[42] Khare D, Singh P and Dubey A K 2022 Interplay of surface polarization charge, dynamic electrical stimulation and compositional modification towards accelerated osteogenic response of NaxK1-xNbO3 piezo-bioceramics *Biomaterials Advances* **140** 213042

[43] Khare D, Basu B and Dubey A K 2020 Electrical stimulation and piezoelectric biomaterials for bone tissue engineering applications *Biomaterials* **258** 120280

[44] Dubey A K and Basu B 2014 Pulsed electrical stimulation and surface charge induced cell growth on multistage spark plasma sintered hydroxyapatite-barium titanate piezobiocomposite *Journal of the American Ceramic Society* **97** 481-9

[45] More N and Kapusetti G 2017 Piezoelectric material–a promising approach for bone and cartilage regeneration *Medical hypotheses* **108** 10-6

[46] Jacob J, More N, Kalia K and Kapusetti G 2018 Piezoelectric smart biomaterials for bone and cartilage tissue engineering *Inflammation and regeneration* **38** 1-11

[47] Srirussamee K, Mobini S, Cassidy N J and Cartmell S H 2019 Direct electrical stimulation enhances osteogenesis by inducing Bmp2 and Spp1 expressions from macrophages and preosteoblasts *Biotechnology and Bioengineering* **116** 3421-32

[48] Das K, Bose S and Bandyopadhyay A 2007 Surface modifications and cell–materials interactions with anodized Ti *Acta biomaterialia* **3** 573-85

[49] Dikici B A, Dikici S, Karaman O and Oflaz H 2017 The effect of zinc oxide doping on mechanical and biological properties of 3D printed calcium sulfate based scaffolds *Biocybernetics and Biomedical Engineering* **37** 733-41

[50] Webb K, Hlady V and Tresco P A 1998 Relative importance of surface wettability and charged functional groups on NIH 3T3 fibroblast attachment, spreading, and cytoskeletal organization *Journal of Biomedical Materials Research: An Official Journal of The Society for Biomaterials, The Japanese Society for Biomaterials, and the Australian Society for Biomaterials* **41** 422-30

[51] Srinath P, Abdul Azeem P and Venugopal Reddy K 2020 Review on calcium silicate-based bioceramics in bone tissue engineering *International Journal of Applied Ceramic Technology* **17** 2450-64

[52] Wu T, Lu T, Shi H, Wang J and Ye J 2023 Enhanced osteogenesis, angiogenesis and inhibited osteoclastogenesis of a calcium phosphate cement incorporated with strontium doped calcium silicate bioceramic *Ceramics International* **49** 6630-45

[53] Pietak A M, Reid J W, Stott M J and Sayer M 2007 Silicon substitution in the calcium phosphate bioceramics *Biomaterials* **28** 4023-32

[54] Maeno S, Niki Y, Matsumoto H, Morioka H, Yatabe T, Funayama A, Toyama Y, Taguchi T and Tanaka J 2005 The effect of calcium ion concentration on osteoblast viability, proliferation and differentiation in monolayer and 3D culture *Biomaterials* **26** 4847-55

[55] Maehira F, Miyagi I and Eguchi Y 2009 Effects of calcium sources and soluble silicate on bone metabolism and the related gene expression in mice *Nutrition* **25** 581-9